Submitted to the 30th International Conference on High-Energy Physics ICHEP2000,
Osaka, Japan, July 2000

Diffractive Jet-Production in Deep-Inelastic e^+p Collisions at HERA

H1 Collaboration

Abstract

A measurement is presented of dijet and 3-jet cross sections in low-$|t|$ diffractive deep-inelastic scattering interactions of the type $ep \rightarrow eXY$, where the photon dissociation system X is separated by a large rapidity gap from a leading low-mass baryonic system Y. Data taken in 1996 to 1997 with the H1 detector at HERA, corresponding to an integrated luminosity of $18.0\ \mathrm{pb}^{-1}$, are used to measure a comprehensive set of single and double differential cross sections in the kinematic range $4 < Q^2 < 80\ \mathrm{GeV}^2$, $x_{I\!P} < 0.05$ and $p_{T,jet} > 4\ \mathrm{GeV}$. The nature of the energy flow not attributed to the dijet system is also investigated. Viewed in terms of the diffractive scattering of parton fluctuations of the photon, the data require the dominance of $q\bar{q}g$ over $q\bar{q}$ states. They constrain the diffractive gluon distribution and require a large fraction of the colorless exchange momentum to be carried by gluons. The data are consistent with factorization of the $x_{I\!P}$ dependence, a Pomeron intercept value of $\alpha_{I\!P}(0) = 1.2$ and a sizeable fraction of events where the virtual photon is resolved. Soft color neutralization models can reproduce the shapes of the differential distributions but underestimate the cross section. A perturbative QCD calculation based on 2-gluon exchange is in agreement with the data at low $x_{I\!P}$ values. The 3-jet cross sections are in excess of the model predictions.

Abstract: 960
Parallel session: 2
Plenary talk: 12

1 Introduction

The observation of deep-inelastic scattering (DIS) events at HERA containing a large gap in the rapidity distribution of the final state hadrons has generated considerable renewed interest in understanding the phenomenon of diffractive scattering or color singlet exchange. Traditionally, such interactions have been described within Regge phenomenology of high energy scattering. With the advent of the electron-proton collider HERA, it has become possible to study the dynamics of diffractive scattering using a point-like, highly virtual photon emitted from the beam electron as a probe. This offers the chance to illuminate the underlying dynamics of diffractive scattering in terms of quantum chromodynamics (QCD).

Apart from measurements of inclusive diffractive scattering at HERA [1–3], it is particularly interesting to focus on those hadronic final states where additional hard scales μ^2 are introduced, for example due to the presence of heavy quarks or high transverse momentum (p_T) jets. The production of high p_T jet final states in diffractive scattering was observed in $p\overline{p}$ collisions [4–6] as well as at HERA [7, 8]. The advantage of diffractive dijet production is the direct sensitivity to the gluon component of the diffractive exchange, which can only be inferred indirectly from scaling violations in the case of inclusive structure function measurements.

In this article, a high statistics measurement of dijet and 3-jet production in color singlet exchange events is presented which was performed with the H1 detector at HERA. Deep-inelastic scattering events ($Q^2 > 4\ \mathrm{GeV}^2$) are selected where the proton (or a low-mass excitation) looses only a small fraction of its incoming momentum and escapes undetected through the beam pipe. Separated from it by a large rapidity gap devoid of hadronic activity, the photon dissociation system X is well contained within the central part of the detector. The selection of events implies that the longitudinal momentum fraction of the proton transferred to the X system ($x_{I\!P}$) is small. In the analysis, events with either at least two or exactly three high p_T jets contained in X are considered.

This article is organized as follows. The kinematics of diffractive scattering at HERA are introduced in section 2. In section 3, an overview of phenomenological models relevant for diffractive jet production is given and the simulation of diffractive events using Monte Carlo generators is described. In section 4, the data selection, the measurement of the jet cross sections and the determination of the systematic uncertainties are presented. The results, expressed in terms of hadron level single and double differential cross sections, are presented and discussed in section 5. The article ends with a summary and final remarks in section 6.

2 Kinematics of Diffractive Scattering at HERA

2.1 Inclusive Diffractive Scattering

Fig. 1 illustrates the generic diffractive process at HERA of the type $ep \to eXY$. At the time when the data presented here were taken, HERA collided $E_e = 27.5\ \mathrm{GeV}$ positrons[1]

---

[1] The word “electron” will be used as a generic term for electrons and positrons throughout the article.

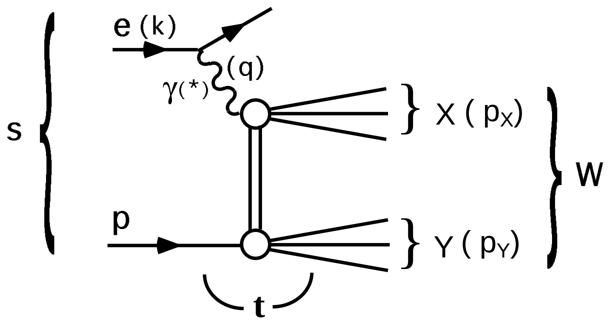

Figure 1: The generic diffractive process at HERA, where the electron (k) emits a photon (q) which interacts with a proton (P) via net color singlet exchange, producing two distinct final state hadronic systems X and Y. Where the masses of X and Y are small, the two systems are separated by a large gap in rapidity.

with protons of $E_p = 820~\mathrm{GeV}$. In deep-inelastic scattering, the incoming electron (with 4-momentum k) emits a virtual photon γ^* (q) which interacts with a proton (P). The usual DIS kinematic variables are defined as

$$Q^2 = -q^2 \; ; \qquad y = \frac{P \cdot q}{P \cdot k} \; ; \qquad x = \frac{-q^2}{2P \cdot q} \; . \tag{1}$$

The squared invariant masses of the electron-proton and photon-proton systems s and W^2 are given by

$$s = \frac{Q^2}{xy} \approx 4E_e E_p \approx (300~\mathrm{GeV})^2 \; ; \qquad W^2 = (q + P)^2 \approx ys - Q^2 \; . \tag{2}$$

If the interaction takes place via color singlet exchange, two distinct hadronic systems of the dissociating photon and proton, X and Y, are produced, with invariant masses M_X and M_Y respectively. In the case where M_X and M_Y are small compared with W, the two systems are separated by a large rapidity gap. The longitudinal momentum fraction of the colorless exchange with respect to the incoming proton $x_{I\!P}$ and the squared four-momentum transferred at the proton vertex t are then defined by

$$x_{I\!P} = \frac{q \cdot (P - p_{\mathrm{Y}})}{q \cdot P} \; ; \qquad t = (P - p_Y)^2 \; , \tag{3}$$

where p_Y is the 4-momentum of Y. In addition, the quantity β is defined as

$$\beta = \frac{x}{x_{I\!P}} = \frac{Q^2}{2q \cdot (P - p_{\mathrm{Y}})} \; . \tag{4}$$

In a partonic interpretation, β is the longitudinal momentum fraction of the colorless exchange carried by the struck quark, in analogy to x in the case of inclusive scattering. In the analysis presented here, the system Y escapes undetected through the proton beam-pipe. Therefore, t and M_Y are not measured and thus integrated over implicitly[2].

---

[2] It is noted that for this analysis $M_Y = M_p$ dominantly.

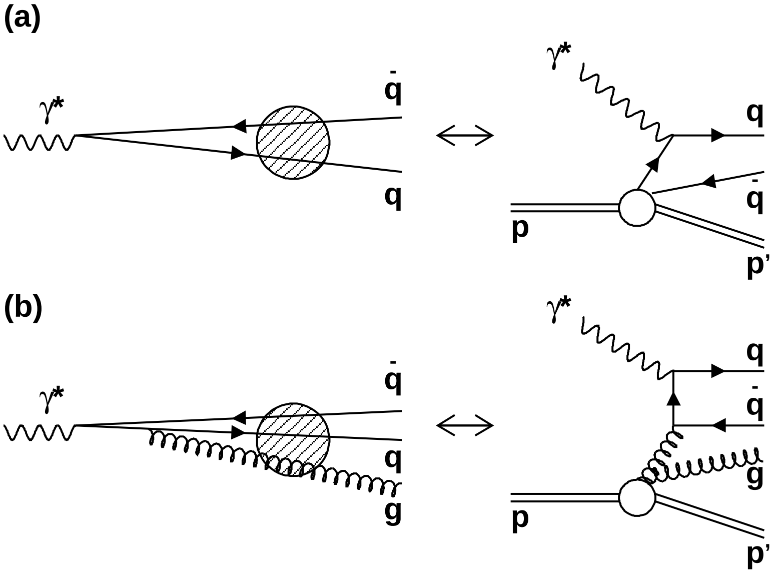

Figure 2: Diffractive scattering, viewed in the proton rest frame (*left*) and the infinite momentum frame (*right*). (*a*) In the proton rest frame, the virtual photon dissociates into a $q\overline{q}$ state, scattering off the proton by color singlet exchange (diffractive quark scattering). (*b*) The emission of an additional gluon forms a $q\overline{q}g$ state (diffractive gluon scattering or Boson-Gluon-Fusion).

2.2 Diffractive Dijet Production

Viewed in the proton rest frame, the virtual photon dissociates into a $q\overline{q}$ pair well before the interaction with the proton (Fig. 2a). The $q\overline{q}$ state is coupled to the elastically scattered proton by a color singlet exchange (diffractive quark scattering). It is expected that for larger values of M_X, corresponding to low values of β, this picture is not sufficient and additional contributions like the radiation of an extra gluon become important, producing an incoming $q\overline{q}g$ system, which is often also modelled as a colour dipole (Fig. 2b). Small size dipole configurations with high transverse momenta are calculable within perturbative QCD, whereas large size, low p_T configurations are similar to soft hadron-hadron scattering.

The diffractive quark scattering process (Fig. 2a) represents the lowest order, i.e. $O(\alpha_s^0)$, diagram. High p_T final states can be produced in leading order QCD, i.e. $O(\alpha_s)$, via the Boson-Gluon-Fusion (BGF) and QCD-Compton (QCDC) processes. Figure (Fig. 2b) corresponds to diffractive Boson-Gluon-Fusion in the proton infinite momentum frame. Because of the non-zero invariant mass $\sqrt{\hat{s}} = M_{12}$ of the two final state partons, a new variable $z_{I\!P}$ is introduced:

$$z_{I\!P} = \beta \cdot \left(1 + \frac{\hat{s}}{Q^2}\right) \ . \tag{5}$$

The interpretation of $z_{I\!P}$ is equivalent to the one of β in the case of the $O(\alpha_s^0)$ diagram. In models where the colorless exchange is attributed an internal structure, it corresponds to the longitudinal momentum fraction of the exchange which takes part in the hard interaction. In such models, diffractive jet-production is directly sensitive to the gluon distribution $g^D(z, \mu^2)$ of the diffractive exchange.

3 Phenomenological Models and Monte Carlo Simulation

In this section, several phenomenological approaches and QCD calculations, attempting to describe diffractive DIS and especially diffractive jet production, will be discussed. The focus will be on those which are compared with the data in section 5.

3.1 Diffractive Parton Distributions

In the leading $\log(Q^2)$ approximation, the cross section for the diffractive process $\gamma^* p \to p' X$ can be written in terms of convolutions of partonic cross sections $\hat{\sigma}^{\gamma^* i}$ with diffractive parton distributions f_i^D, representing probability distributions for a parton in the proton under the additional constraint that the proton remains intact with particular values of $x_{I\!P}$ and t:

$$\frac{d\sigma(x, Q^2, x_{I\!P}, t)^{\gamma^* p \to p' X}}{dx_{I\!P} dt} = \sum_i \int_x^{x_{I\!P}} dy \; \hat{\sigma}(x, Q^2, y)^{\gamma^* i} \left(\frac{df_i^D(y, x_{I\!P}, t)}{dx_{I\!P} dt} \right) . \tag{6}$$

This factorization formula holds for fixed values of x, $x_{I\!P}$ and t and is exactly valid in the limit $Q^2 \to \infty$, where higher twist contributions become negligible. This ansatz was introduced in [9] and applied to hard diffraction in [10]. The proof of Eq. (6) for inclusive diffractive lepton-hadron scattering was given in [11] in the framework of a scalar model and in [12] for full QCD. The partonic cross sections are identical to those in non-diffractive scattering. The diffractive parton distributions however, which should obey the DGLAP [13] evolution equations, are not known from first principles. Recently, there have been approaches to calculate the distributions at the starting scale μ_0^2 of the QCD evolution under certain assumptions. In [14], the case of a $q\bar{q}$-pair made of heavy quarks coupling to a small-size hadron has been studied, which is perturbatively calculable. A different approach is the Semiclassical model by Buchmüller, Gehrmann and Hebecker [15], based on the opposite extreme of a very large hadron. In spite of the different assumptions, both approaches give rather similar results for the diffractive parton distributions: The parton distributions follow the same general behavior at the endpoints $z = 0$ and $z = 1$ and the gluon distribution dominates.

3.2 Resolved Pomeron Model and Pomeron Parton Distributions

The application of Regge phenomenology for soft hadronic high energy interactions to the concept of diffractive parton distributions leads naturally to the Ingelman-Schlein model of a resolved Pomeron with a partonic structure [16] invariant under changes in $x_{I\!P}$ and t. The diffractive parton distributions then factorize into a flux factor $f_{I\!P/p}$ and Pomeron parton distributions $f_i^{I\!P}$:

$$\frac{df_i^D(x, Q^2, x_{I\!P}, t)}{dx dQ^2 dx_{I\!P} dt} = f_{I\!P/p}(x_{I\!P}, t) \; f_i^{I\!P}(\beta = x/x_{I\!P}, Q^2) . \tag{7}$$

The universal flux factor describes the probability to find a colorless state in the proton, the "Pomeron", as a function of $x_{I\!P}$ and t.

The H1 collaboration has interpreted their measurements of inclusive diffraction (presented in the form of a diffractive structure function $F_2^{D(3)}$) in terms of such a model [2]. For the range of $x_{I\!P}$ under study, it turned out to be necessary to consider more generally contributions from sub-leading Reggeon exchanges as well as the pomeron:

$$F_2^{D(3)}(\beta, Q^2, x_{I\!P}) = \int dt\; f_{I\!P/p}(x_{I\!P}, t) \cdot F_2^{I\!P}(\beta, Q^2) \;+\; \int dt\; f_{I\!R/p}(x_{I\!P}, t) \cdot F_2^{I\!R}(\beta, Q^2)\;. \quad (8)$$

$F_2^{I\!P}(\beta, Q^2)$ and $F_2^{I\!R}(\beta, Q^2)$ are the Pomeron and Reggeon structure functions. The flux factors for the Pomeron and Reggeon exchanges were parameterized in a Regge-inspired form:

$$f_{\{I\!P,I\!R\}/p}(x_{I\!P}, t) = C_{\{I\!P,I\!R\}}\; {x_{I\!P}}^{1-2\alpha_{\{I\!P,I\!R\}}(t)}\; e^{b_{\{I\!P,I\!R\}}t}\;. \quad (9)$$

From mixed Regge and QCD fits to the measured data, a value for the Pomeron intercept $\alpha_{I\!P}(0)$ and parameterizations of the Pomeron parton densities were obtained. The resulting value of $\alpha_{I\!P}(0) = 1.203 \pm 0.020(stat.) \pm 0.013(syst.) \pm 0.030(model)$ is significantly higher than that obtained from soft hadronic interactions, where $\alpha_{I\!P}(0) \sim 1.08$ [17]. The parton densities extracted for the Pomeron are dominated by gluons, which carry $80 \ldots 90\%$ of the Pomeron momentum.

3.3 Colour Dipole and 2-gluon Exchange Models

In the proton rest frame, the virtual photon splits into a $q\bar{q}$ or $q\bar{q}g$ system well in advance of the target. These states are then scattered off the proton by net color singlet exchange. Many properties of the diffractive final state can be deduced from a knowledge of the partonic wave functions of the photon alone. The β distribution for example is largely determined by the photon wave functions and depends only weakly on the way these are coupled to the proton. In a recent QCD motivated parameterisation [18] longitudinally and transversely polarized $q\bar{q}$ states contribute at high and medium values of β respectively, whereas the $q\bar{q}g$ state originating from a transversely polarized photon is dominant at low β (i.e. high M_X). The diffractive coupling of these states to the proton is not known a priori. However, the simplest realization of a net color singlet exchange at the parton level is a pair of gluons with opposite color charges [19]. The cross section is then closely related to the square of the unintegrated gluon distribution of the proton $\mathcal{F}(x, k_i^2)$. We will focus here on two recent models based on the ideas of diffractive scattering of partonic fluctuations of the photon and two gluon exchange. Other approaches can be found in [20], for example.

In impact parameter space, the condition of k_T-factorization is equivalent to the factorization of the $\gamma^* p$ cross section into an effective photon dipole wave function $|\Psi|^2$ and the dipole cross section $\hat{\sigma}$ [21]. The diffractive cross section depends on the square of the dipole cross section. Investigating diffractive final states with varying transverse momenta, for example by studying jets, probes the dipole cross section as a function of the dipole size in the transition region between Regge phenomenology and perturbative QCD. In the 'Saturation' model by Golec-Biernat and Wüsthoff [22], an Ansatz for the dipole cross section is made which interpolates between the perturbative and non-perturbative regions of $\sigma^{\gamma^* p}$. This model is able to give a reasonable description of $F_2(x, Q^2)$ at low x, which determines the free parameters of the model (only 4). The diffractive structure function $F_2^{D(3)}$ is then predicted and also described reasonably well. The model predicts a constant ratio of the diffractive over the inclusive cross sections. The calculation of the $q\overline{q}g$ cross section for medium β is made under the assumption of strong k_T ordering of the final state partons, corresponding to $k_T^{(g)} \ll k_T^{(q,\overline{q})}$.

Cross sections for diffractive $q\overline{q}$ and $q\overline{q}g$ production by 2-gluon exchange have been calculated by Bartels, Lotter and Wüsthoff ($q\overline{q}$) [23] and by Bartels, Jung and Wüsthoff ($q\overline{q}g$) [24]. The calculation of the $q\overline{q}g$ final state is performed in the low-β or “triple Regge” limit, taking also configurations without strong k_T ordering into account. The calculations require high p_T of all outgoing partons. Thus, this model is particularly suited for diffractive jet production.

3.4 Soft Color Neutralization Models

An alternative approach to diffractive DIS, not based on special concepts for diffraction but closely related to inclusive scattering, is given by soft color neutralization models. These models naturally lead to very similar properties of inclusive and diffractive DIS final states.

One example is Soft Color Interaction (SCI) model by Edin, Ingelman and Rathsman [25]. In its original version, the hard interaction in diffractive DIS was treated identically to that in inclusive DIS. Diffraction enters through soft color rearrangements between the outgoing partons, leaving their momentum configuration unchanged. If two color singlet systems are produced by such a mechanism, the hadronic final state can exhibit a visible rapidity gap. There is only one additional free parameter, namely the universal probability for color rearrangements to occur, which is fixed by a fit to $F_2^{D(3)}$. The model has been refined recently by making the color rearrangement probability proportional to the difference in the generalized areas of the string configurations before and after the rearrangement [26].

Another approach is the Semiclassical model [15], a non-perturbative model which was already mentioned in section 3.1. Viewed in the proton rest frame, $q\overline{q}$ and $q\overline{q}g$ configurations scatter off a superposition of soft color fields originating from the proton. Those configurations which emerge in a net color singlet configuration contribute to the diffractive cross section. A parameterization of diffractive parton distributions is derived from a combined 4 parameter fit to the inclusive and diffractive structure functions F_2 and F_2^D at low x.

3.5 Monte Carlo Simulation

Monte Carlo simulations are used to determine the corrections to be applied to the measured data to compensate for the limited efficiencies, acceptances and resolutions of the detector. The generated Monte Carlo events are subjected to a detailed simulation of the H1 detector and passed through the same reconstruction and analysis chain as the measured data.

The main Monte Carlo generator used for this purpose is RAPGAP 2.08 [27]. Events are generated according to a resolved (partonic) Pomeron model. Contributions from Pomeron and sub-leading meson exchanges are included. The parameterizations of the Pomeron and meson flux factors and parton distributions are taken from the H1 analysis of $F_2^{D(3)}$ [2] (see

Eq. 8). The Pomeron and meson trajectories and slope parameters are $\alpha_{I\!P}(t) = 1.20 + 0.26t$, $b_{I\!P} = 4.6\ \mathrm{GeV}^{-2}$ and $\alpha_{I\!R}(t) = 0.50 + 0.90t$, $b_{I\!R} = 2.0\ \mathrm{GeV}^{-2}$ respectively. The Pomeron parton distributions are the "flat gluon" (or "fit 2") parameterizations extracted from the leading order QCD fits to $F_2^{I\!P}(\beta, Q^2)$. The meson structure function is taken from a parameterization of the pion [28]. The renormalization and factorization scales are set to $\mu^2 = Q^2 + p_T^2$, where p_T is the transverse momentum of the partons emerging from the hard scattering. The parton distributions are convoluted with hard scattering matrix elements to leading order in QCD. Transverse momenta of the incoming partons are not included in the calculation of the cross sections. Outgoing charm quarks are produced in the massive scheme via Boson-Gluon-Fusion. For the production of light quarks, a lower cutoff in p_T^2 is introduced in the $\mathcal{O}(\alpha_s)$ QCD matrix elements to avoid divergences in the calculation. Higher order QCD diagrams are approximated with parton showers in the leading $\log(\mu)$ approximation (MEPS) [29]. Hadronisation is simulated using the Lund string model [30].

In RAPGAP, a contribution of events where the virtual photon γ^* is resolved and assigned an internal partonic structure can also be simulated. The parton densities for the virtual photon are taken from the SAS-2D [31] parameterization, which has been found to give a reasonable description of non-diffractive dijet production at low Q^2 in a previous H1 measurement [32].

Monte Carlo generators are also used to compare the measured hadron level cross sections to the predictions of the phenomenological models and QCD calculations presented in the previous sections. RAPGAP is used to obtain the predictions of the resolved Pomeron model with different Pomeron intercept values and parton distributions. It also contains implementations of the Saturation model [33] and the Semiclassical model [34] as well as the 2-gluon exchange model by Bartels et al. Both versions of the Soft Color Interaction (SCI) model are implemented in the LEPTO $6.5.2\beta$ generator [35], which was used for the comparisons with these models.

4 Experimental Procedure

The analysis presented in this article is based on H1 data corresponding to an integrated luminosity of $18.0\ \mathrm{pb}^{-1}$. The data were taken in the years 1996 and 1997, when HERA collided 820 GeV protons with 27.5 GeV positrons. A detailed description of the measurement can be found in [36].

4.1 H1 Detector

The H1 detector is described in detail elsewhere [37]. Here, we will give a brief description of the detector components most relevant for the analysis. The z-axis of the H1 coordinate system corresponds to the nominal beam axis such that positive z values indicate the direction of the outgoing proton beam which is often referred to as the "forward" direction[3].

The beam pipe is surrounded by the tracking system. Two large concentric drift chambers (CJC), located within a solenoidal magnetic field of 1.15 T, measure the trajectories of charged

---

[3] This direction corresponds to positive values of the pseudorapidity $\eta = -\ln\tan\theta/2$.

particles and their momenta in the range $-1.5 < \eta < 1.5$ with a precision of $\sigma(p)/p < 0.01 \cdot p/\mathrm{GeV}$. Energies of final state particles are measured in a highly segmented Liquid Argon (LAr) calorimeter covering the range $-1.5 < \eta < 3.4$, surrounding the tracking detectors. The energy resolution is $\sigma(E)/E \approx 11\%/\sqrt{E}$ for electro-magnetic showers and $\sigma(E)/E \approx 50\%/\sqrt{E}$ for hadrons. The systematic uncertainty on the hadronic energy measurement in the LAr is 4%. The "backward", i.e. outgoing electron beam, direction ($-4.0 < \eta < -1.4$) is covered by a lead / scintillating fibre calorimeter (SPACAL) with electro-magnetic and hadronic sections. In this measurement, the scattered DIS electron is identified in the SPACAL with an energy resolution between 0.3% for kinematic peak electrons ($E_{e'} = 27.5$ GeV) and 2.0% at low energies ($E_{e'} = 8$ GeV). The energy resolution of the hadronic part of the SPACAL is 7%. In front of the SPACAL, the Backward Drift Chamber (BDC) provides track segments of charged particles with a resolution of $\sigma_{dr} = 0.4$ mm and $\sigma_{rd\phi} = 0.8$ mm.

Beam induced backgrounds are suppressed using a time-of-flight scintillator system (TOF). The ep luminosity is determined by comparison of the QED cross section for the bremsstrahlung reaction $ep \rightarrow ep\gamma$ with the measured event rate in a photon tagger calorimeter close to the beam pipe at $z = -103$ m with a precision of 2%.

To enlarge the coverage for hadronic activity up to pseudorapidities of $\eta = 7.5$ in the region of the outgoing proton, the Forward Muon Detector (FMD) and the Proton Remnant Tagger (PRT) are used for the analysis. The FMD is located at $z = 6.5$ m and covers the pseudorapidity range $1.9 < \eta < 3.7$ directly. It also has sensitivity to larger η values because of secondary scattering. The Proton Remnant Tagger (PRT), a set of scintillators surrounding the beam pipe at $z = 26$ m, can tag hadrons in the region $6 < \eta < 8$.

4.2 Data Selection

Deep-inelastic scattering events are triggered by an electro-magnetic energy cluster in the SPACAL with $E_{e'} > 8$ GeV in coincidence with a reconstructed CJC track associated to the event vertex. Due to the track requirement, the trigger efficiency varies for the selected events between 80 and 90%, depending on the kinematics. DIS electron candidates are selected in the angular range $156^o < \theta_{e'} < 176^o$. Various cuts are applied on these candidates in order to select electrons and reject background originating from photons and hadrons. Among these are requirements on the width of the shower, the containment within the electro-magnetic part of the SPACAL and the existence of a reconstructed track segment in the BDC pointing from the vertex to the electron candidate. The z coordinate of the reconstructed vertex is required to lie within ± 35 cm ($\pm \sim 3\sigma$) of the nominal interaction point. To suppress events with initial state QED radiation, the summed $E - p_Z$ of all reconstructed final state particles including the electron[4] has to be greater than 35 GeV. The DIS kinematic variables are calculated from the polar angle and energy measurements of the scattered electron:

$$Q^2 = 4E_eE_{e'}\cos^2\frac{\theta_{e'}}{2}\ ; \qquad y = 1 - \frac{E_{e'}}{E_e}\sin^2\frac{\theta_{e'}}{2}\ . \tag{10}$$

---

[4] For DIS events fully contained in the detector, the total $E - p_Z$ satisfies 55 GeV.

Events which fulfill

$$4 < Q^2 < 80\ \mathrm{GeV}^2\ ; \qquad 0.1 < y < 0.7 \tag{11}$$

are selected.

The selection of diffractive events is based on requirements on the absence of hadronic activity in the outgoing proton region. No signal above noise levels is allowed in the FMD and PRT detectors. The most forward part ($\eta > 3.2$) of the LAr calorimeter has to be devoid of hadronic energy clusters with energies $E > 400\ \mathrm{MeV}$. This selection ensures that the photon dissociation system X is well contained within the central part of the H1 detector and is separated by a large rapidity gap covering at least $3.2 < \eta < 7.5$ from the Y system, which escapes undetected through the beam pipe. This imposes the constraint $M_Y < 1.6$ GeV and $|t| < 1.0\ \mathrm{GeV}^2$.

The X system, measured in the LAr and SPACAL calorimeters together with the CJC, is reconstructed using a method that combines calorimeter clusters and tracks carefully avoiding double counting [38]. Its mass is then calculated according to

$$M_X^2 = (\textstyle\sum_i E_i)^2 - (\textstyle\sum_i \mathbf{p}_i)^2\ , \tag{12}$$

were the sum runs over all reconstructed objects except for the scattered electron. W^2 is calculated according to Eq. (2). $x_{I\!P}$ and β are then computed by

$$x_{I\!P} = \frac{Q^2 + M_X^2}{Q^2 + W^2}\ ; \qquad \beta = \frac{Q^2}{Q^2 + M_X^2}\ . \tag{13}$$

The correlation between the hadron level and detector level values of $x_{I\!P}$, as obtained from the Monte Carlo simulations, is shown in Fig. 3a. The resolution in $\log x_{I\!P}$ is 8%. A cut

$$x_{I\!P} < 0.05 \tag{14}$$

is applied to suppress contributions from non-diffractive scattering and secondary exchanges.

The 4-vectors of the hadronic final state particles associated to the X system are then Lorentz-transformed to the $\gamma^* p$ center-of-mass frame[5], where they are subjected to the CDF cone jet algorithm [39] with a cone radius of $R_{cone} = \sqrt{\Delta\eta^2 + \Delta\phi^2} = 1.0$. Transverse energies and momenta are calculated with respect to the $\gamma^* p$ axis. Events with either at least two or exactly three jets with transverse momenta $p^*_{T,jet} > 4$ GeV are selected for the dijet and 3-jet samples respectively. The jets are required to lie within the region of $-1.0 < \eta^{lab}_{jet} < 2.2$ to ensure a good containment within the LAr calorimeter. In Fig. 3b, the correlation between the hadron level and the reconstructed values of $p^*_{T,jets}$, the mean dijet transverse momentum, is shown. The resolution is 14%. The final event selection yields approx. 2.500 dijet and 130 3-jet events.

4.3 Cross Section Measurement

The measured distributions are corrected for detector acceptances, efficiencies and resolutions using the RAPGAP program (see section 3.5), interfaced to HERACLES [40] to take QED

---

[5] This frame is also called the "hadronic center-of-mass frame".

Cross Section Definition
$4 < Q^2 < 80\ \mathrm{GeV}^2$ $0.1 < y < 0.7$
$x_{I\!P} < 0.05$ $M_Y < 1.6\ \mathrm{GeV}$ $\lvert t\rvert < 1.0\ \mathrm{GeV}^2$
$N_{\mathrm{jets}} \geq 2$ or $N_{\mathrm{jets}} = 3$ $p^*_{T,jet} > 4\ \mathrm{GeV}$ $-3 < \eta^*_{jet} < 0$

Table 1: The kinematic range in which the cross sections are measured.

corrections into account. The simulations give a very good description of all relevant kinematic distributions of the selected dijet and 3-jet events. Smearing in $x_{I\!P}$ is taken into account up to $x_{I\!P} = 0.2$ in RAPGAP. Migrations from $x_{I\!P} > 0.2$ or from large values of $M_Y > 5$ GeV are covered by a RAPGAP simulation of non-diffractive DIS. This contribution is at the level of 5% averaged over all bins and is concentrated at large $x_{I\!P}$. An additional factor of $-2.3 \pm 5.0\%$ is applied to account for the net smearing about the $M_Y = 1.6$ GeV boundary which is not covered by RAPGAP because it only generates elastically scattered protons. The factor has been determined using the DIFFVM [42] simulation of proton dissociation. Furthermore, a correction of $7.8 \pm 1.9\%$ takes into account diffractive events rejected due to fluctuations in the amount of noise in the FMD detector. The correction has been determined using randomly triggered events.

The cross sections are corrected to the Born level. QED corrections are small for most of the data points, typically at the level of 5%. The data are corrected using a bin-to-bin correction method. The bin purities and stabilities are typically of the order of 50 to 60% and it is ensured that they exceed 30% in every bin of the resulting cross sections.

The corrected hadron level cross sections are defined in terms of a model independent definition of rapidity gap events. Two systems X and Y are defined by searching for the largest gap in rapidity among the hadrons in the $\gamma^* p$ center-of-mass frame (Fig. 1). No $\eta_{\max}$ or similar cuts are imposed in the definition of the measured cross sections. The full definition of the hadronic cross sections is given in Tab. 1. The cross section definition in terms of jet pseudorapidities in the hadronic center-of-mass frame $-3 < \eta^*_{jet} < 0$ approximately matches the $-1 < \eta^{lab}_{jet} < 2.2$ cut for the selected events.

Fig. 4 shows the transverse energy flow around the jet axes for the dijet sample. For the jet profiles in η and ϕ, only transverse energies within one unit in azimuth and pseudorapidity are included in the plots respectively. The jet profiles for backward and forward jets are shown separately in Figs. 4a,c and b,d respectively. The data exhibit a clear back-to-back dijet structure in azimuth. The energy flow is well described by the RAPGAP simulation.

4.4 Analysis of Systematic Uncertainties

The following sources of systematic uncertainties contribute to the total systematic error on the measured cross sections. The experimental uncertainties taken into account are:

1. The uncertainties on the hadronic calibrations of the LAr and SPACAL calorimeters are $\pm 4\%$ and $\pm 7\%$ respectively. Both influence the measured values of $p^*_{T,jet}$ and $x_{I\!P}$ and result in uncertainties in the measured cross sections of up to 10% (with a mean value of 5%) for the LAr and 0.5% for the SPACAL.

2. The uncertainties on $E_{e'}$ and $\theta_{e'}$ propagate into the reconstruction of Q^2, y and W and the definition of the $\gamma^* p$ axis for the boost into the $\gamma^* p$ frame. The error on the polar angle measurement of the scattered positron in the SPACAL is ± 1 mrad, leading to a systematic error of 1% to 2%. The uncertainty on the electron energy measurement, which is 0.3% at the kinematic peak ($E_{e'} = 27.5$ GeV) and increases to 2% at $E_{e'} = 8$ GeV, results in a systematic error between $\pm 1\%$ and $\pm 5\%$, depending on the kinematics.

3. The uncertainty on the fraction of energy of the reconstructed hadronic objects carried by tracks is $\pm 3\%$, leading to a systematic error in the range 1% to 5%.

4. The uncertainties on the determinations of the trigger efficiency and the ep luminosity affect the total normalization by 5% and 2% respectively.

5. There is an uncertainty of 25% on the fraction of rejected events due to noise in the FMD detector, which translates into a 2% error on the measured cross sections.

The corrections applied to the measured data are affected by the following uncertainties:

6. The uncertainty on the number of background events migrating into the sample from $x_{I\!P} > 0.2$ or $M_Y > 5$ GeV is estimated as $\pm 25\%$, leading to a 1% to 3% systematic error, with the biggest values at large $x_{I\!P}$.

7. A $\pm 5\%$ uncertainty arises from the M_Y smearing correction. It is estimated by:
   (a) Variation of the ratio of proton elastic to proton dissociation cross sections to either 1:2 or 2:1
   (b) Variation of the generated M_Y distribution in DIFFVM by $1/M_Y^{2.0\pm 0.3}$
   (c) Variation of the t dependencies in the simulations by changing the slope parameter by ± 1 GeV^{-2} and ± 2 GeV^{-2} in the proton dissociation and proton elastic simulations respectively
   (d) Variation of the efficiencies of the forward detectors FMD and PRT by $\pm 4\%$ and $\pm 25\%$ respectively

8. There is an uncertainty on the calculation of the QED radiative corrections of $\pm 5\%$, originating from the limited statistics of the Monte Carlo event samples.

9. The use of different approximations for higher order QCD diagrams, the parton shower model (MEPS) or the color dipole model (CDM) as implemented in the ARIADNE program [41], for the determination of the correction factors leads to a $\pm 3\%$ uncertainty on the resulting cross sections.

10. The model dependence of the acceptance and migration corrections was estimated by varying the shapes of kinematic distributions in the simulations:

   (a) Variation of the $z_{I\!P}$ distribution by $z_{I\!P}^{\pm 0.2}$ and $(1 - z_{I\!P})^{\pm 0.2}$
   (b) Variation of the p_T distribution by $(1/p_T)^{\pm 0.5}$
   (c) Variation of the $x_{I\!P}$ distribution by $(1/x_{I\!P})^{\pm 0.2}$
   (d) Variation of the t distribution by $e^{\pm 2t}$
   (e) Reweighting of the η_{jet} distribution to that observed in the data

   The resulting systematic uncertainties range between $\pm 6\%$ and $\pm 13\%$, where the largest contributions originate from the assumed shape of the $x_{I\!P}$ and η distributions in the simulation.

11. The lower p_T-cutoff chosen to avoid collinear divergences in the leading order QCD matrix elements in RAPGAP is relatively high ($p_T^2 > 9\ GeV^2$) with respect to the experimental cut of $p^{*2}_{T,jet} > 16\ \mathrm{GeV}^2$, Studying the dependence of the cross sections on the cutoff value results in an additional uncertainty of $\pm 5\%$.

The total systematic error has been evaluated in each bin of the cross sections which are presented by adding all individual systematic errors in quadrature. The systematic error dominates the total uncertainty on the dijet cross sections. In the case of 3-jet production, the statistical errors are more important.

5 Results

This section presents the obtained differential cross sections for dijet and 3-jet production in diffractive DIS in the kinematic region specified in Tab. 1 . The obtained cross sections are shown in Figs. 6-13 . The inner error bars correspond to the statistical error, the outer error bars represent the quadratic sum of the statistical and systematic errors.

5.1 General Properties of the Dijet Data

In Fig. 5a, the uncorrected average transverse energy flow per event for the dijet sample is shown in the $\gamma^* I\!P$ center-of-mass frame[6] as a function of the pseudorapidity η^+. Positive values of η^+ correspond to the Pomeron[7] hemisphere, negative values to the photon hemisphere. Comparing the total energy flow to that where only particles not belonging to the two highest p_T jets contribute, the data exhibit considerable additional hadronic energy not associated with the jets. This additional energy is distributed in both hemispheres with a certain preference for the Pomeron hemisphere. In order to examine the sharing of energy within the X system on an event-by-event basis, Fig. 5b shows the uncorrected correlation between the dijet invariant mass squared M_{12}^2 and the total diffractive mass squared M_X^2. Except for a small subset of the events at low M_X, only a fraction of the available energy of the X system is contained in the dijet system. Typically, a significant amount of additional energy is present which is not associated

---

[6] This frame is equivalent to the rest frame of X.

[7] The term “Pomeron” is used synonymously for the colorless exchange here.

with the jets, leading to $M_{12}^2 < M_X^2$. Even taking into account the effects of hadronisation and detector resolution, this observation suggests the dominance of $q\overline{q}g$ states over $q\overline{q}$ states alone.

Figs. 6 and 7 present differential dijet cross sections as functions of the following observables: The photon virtuality Q^2, the mean dijet transverse momentum $p^*_{T,jets}$, defined as

$$p^*_{T,jets} = \frac{1}{2}\left(p^*_{T,1} + p^*_{T,2}\right) \ , \qquad (15)$$

the $\gamma^* p$ invariant mass W, the mean dijet pseudorapidity in the laboratory frame $\langle\eta\rangle^{lab}_{jets}$, defined as

$$\langle\eta\rangle^{lab}_{jets} = \frac{1}{2}\left(\eta^{lab}_1 + \eta^{lab}_2\right) \ , \qquad (16)$$

and the $x_{I\!P}$ and β variables. The Q^2 and $p^*_{T,jets}$ distributions are steeply falling. Due to the selection of events with $Q^2 > 4$ GeV^2 and $p^{*2}_{T,jets} > 16$ GeV^2, the relation $p_T^2 > Q^2$ holds for the bulk of the data. The W range is $90 < W < 260$ GeV. The $x_{I\!P}$ distribution shows a rising behavior from the lowest accessible values of 0.003 up to the cut value of 0.05 . For kinematic reasons, the dijet measurement is restricted to larger $x_{I\!P}$ values compared to inclusive measurements. The β range covered by the measurement extends down to almost 10^{-3}, lower than accessed by the measurements of $F_2^{D(3)}$. The measured cross sections are generally well described by the RAPGAP simulation used to correct the data, except for the $\langle\eta\rangle^{lab}_{jets}$ distribution, which indicates that the measured jets typically have slightly larger pseudorapidities compared to the simulations.

Fig. 8 presents the cross section as a function of $z_{I\!P}^{(jets)}$, calculated from M_X, Q^2 and the invariant dijet mass M_{12}:

$$z_{I\!P}^{(jets)} = \frac{Q^2 + M_{12}^2}{Q^2 + M_X^2} \ . \qquad (17)$$

M_{12} is calculated from the massless jet 4-vectors. Monte Carlo studies show that the resolution in $z_{I\!P}$ is 25% (see Fig. 3c) and that a good correlation between $z_{I\!P}^{(jets)}$ and the true value of $z_{I\!P}$ exists. In loose terms, this observable measures the fraction of the hadronic final state energy of the X system which is contained in the two jets. Exclusive $q\overline{q}$ final states, which at the parton level satisfy $z_{I\!P} = 1.0$, can be smeared down to $z_{I\!P}^{(jets)}$ values of around 0.6 because of fragmentation and jet resolution effects. The shape of the measured $z_{I\!P}^{(jets)}$ distribution thus confirms the observation that $q\overline{q}g$ states dominate over $\overline{q}q$ states.

5.2 Interpretation within a Partonic Pomeron Model

A model which has been applied quite frequently in the past to diffractive scattering data from HERA is the Ingelman-Schlein model as described in section 3.2. It has previously been found that Pomeron parton densities dominated by gluons proved successful to describe not only inclusive measurements of the diffractive structure function [1–3] but also more exclusive hadronic final state analyses performed by H1 and ZEUS [43, 44], as well as first results on dijet production reported by H1 [7]. The free parameters of the model to which dijet production is most sensitive are the Pomeron intercept $\alpha_{I\!P}(0)$ and the Pomeron gluon distribution $g_{I\!P}(z, \mu^2)$. The sub-leading Reggeon contribution and the Pomeron quark distribution are well constrained by the inclusive $F_2^{D(3)}$ measurement.

The measured distribution of $z_{I\!P}^{(jets)}$ (Fig. 8), corresponding to the momentum fraction of the colorless exchange transferred to the dijet system, is shown together with predictions based on the two gluon distributions obtained from the scaling violation analysis of $F_2^{I\!P}(\beta, Q^2)$ in [2]. The gluon distributions shown are evaluated at a scale $\mu^2 = Q^2 + p_T^2 = 42\ \mathrm{GeV}^2$, representing the mean value of the selected events. The dijet data have a strong sensitivity to the shape of the gluon distribution. Especially in the region of large $z_{I\!P}$ or β, it is not much constrained by the inclusive measurements, where data with $\beta > 0.65$ were excluded from the QCD analysis. If the "flat gluon" or "fit 2" gluon density is used, a very good agreement with the data is achieved. The "peaked gluon" or "fit 3" parameterization leads to an overestimate of the dijet cross section at high values of $z_{I\!P}^{(jets)}$. The model is also able to give a very good description of the other differential distributions. This can be interpreted as support for a Pomeron structure strongly dominated by gluons. Fig. 9a shows the $z_{I\!P}^{(jets)}$ cross section in four bins of the factorization scale $\mu^2 = Q^2 + p_T^2$. Even in this double differential view, the resolved Pomeron model with parton densities evolving according to the DGLAP equations gives a very good description of the data. The "peaked gluon" solution of the H1 QCD fits overestimates the cross section at high $z_{I\!P}^{(jets)}$ in all regions of μ^2.

The Pomeron intercept $\alpha_{I\!P}(0)$, controls the energy or $x_{I\!P}$ dependence of the cross section. In the predictions of the resolved Pomeron model shown in Figs. 6-9, a value of $\alpha_{I\!P}(0) = 1.2$ is used, taken from the H1 analysis of $F_2^{D(3)}$ [2]. Since the value of $\alpha_{I\!P}(0)$ has been shown to be different at high Q^2 than in soft interactions, it is interesting to investigate whether further variation takes place with the additional hard scale introduced in the dijet sample. In Fig. 7a, the effect on the predicted dijet cross section is shown if $\alpha_{I\!P}(0)$ is changed to the "soft Pomeron" value of 1.08 or to 1.4. The normalization of the Pomeron cross section with a changed value of $\alpha_{I\!P}(0)$ is chosen such that the visible dijet cross section is kept fixed. If the intercept is set to 1.08, the data are underestimated at low $x_{I\!P}$, whereas at high $x_{I\!P}$ the model is above the data. If the intercept is increased from 1.2 to 1.4, the opposite effect is observed. The dijet data therefore suggest a value for $\alpha_{I\!P}(0)$ that is close to that measured from inclusive diffraction in a similar Q^2 region.

In Fig. 9b, the data are used to test Regge factorization, i.e. the factorization of the cross section into a Pomeron probability distribution in the proton and a cross section for the interaction between the Pomeron and the electron. The $z_{I\!P}^{(jets)}$ cross section is measured in four bins of $x_{I\!P}$. A substantial dependence of the shape of the $z_{I\!P}^{(jets)}$ distribution on $x_{I\!P}$ is observed, which is dominantly a kinematic effect because $x_{I\!P}$ and $z_{I\!P}^{(jets)}$ are connected via the relation

$$x_p^{(jets)} = x_{I\!P} \cdot z_{I\!P}^{(jets)} \ , \tag{18}$$

where $x_p^{(jets)}$ denotes the proton momentum fraction which enters the hard process. It is thus only possible to draw conclusions from a comparison of the cross sections with Monte Carlo models based either on the assumption of Regge factorization or not. Again, the factorizing resolved Pomeron model describes the distributions well. Also the Saturation model, in which Regge factorisation is not incorporated by construction, is able to roughly reproduce the data, if a constant scale factor of 2.4 is applied. Thus, at the present level of precision firm conclusions are difficult to draw. However, interpreting Fig. 9b in terms of the Pomeron intercept and the gluon distribution within the resolved Pomeron model, it is clear that there is little freedom to change $\alpha_{I\!P}(0)$ and accommodate this by adjusting the gluon distribution or vice versa.

5.3 Resolved Virtual Photons and non k_T-ordered Contributions

Figs. 6,7 and 8 indicate that the description of the dijet data can be further improved if an additional contribution from resolved virtual photons is added. Here, the virtual photon has an internal partonic structure. For the parton densities of the photon, the SaS-2D [31] parameterization was chosen, which lead to a good description of an earlier measurement of inclusive dijet production at low Q^2 by H1 [32].

Fig. 10 presents cross sections for two observables which are particularly suited to interpret the data in terms of direct and resolved photon contributions. Similar to real photoproduction analyses (see e.g. [45]), a quantity x_γ is defined as the momentum fraction of the photon which enters the hard scattering interaction. If the 4-vector of the parton from the photon is labeled u, x_γ is defined as

$$x_\gamma = \frac{P \cdot u}{P \cdot q} \, . \tag{19}$$

Direct photon events satisfy $x_\gamma = 1$ by definition. Events where the photon is resolved have $x_\gamma < 1$. At the hadron level, an observable $x_\gamma^{(jets)}$ can be constructed by measuring the ratio of the summed $E - p_Z$ of the two jets over the total $E - p_Z$:

$$x_\gamma^{(jets)} = \frac{\sum_{jets} E - p_Z}{\sum_{all} E - p_Z} \, . \tag{20}$$

$x_\gamma^{(jets)}$ is reconstructed with a resolution of 12% (see Fig. 3d). The $x_\gamma^{(jets)}$ distribution of the data, shown in Fig. 10a, is peaked at values around 1 but also shows a sizeable fraction of the events at lower values. The resolved Pomeron model including direct photon contributions alone describes only the high $x_\gamma^{(jets)}$ region but is significantly lower than the data at low values of $x_\gamma^{(jets)}$. It is not zero however because of migrations from the true value of x_γ to the hadron level quantity $x_\gamma^{(jets)}$. If the contribution from resolved photons is included, which increases the total dijet cross section by 17%, a much improved agreement with the data is archived.

It is also possible to look into the part of the hadronic final state not associated to the two highest p_T jets. In the $\gamma^* I\!P$ center-of-mass frame, the $\eta^+ = 0$ plane defines two hemispheres associated with the outgoing photon and Pomeron directions. In addition to QCD radiation and the possible presence of a third jet, hadronic final state particle production in the two hemispheres can originate from possible photon and Pomeron remnants. In order to further investigate the possible presence of a photon remnant, a new observable $E_{rem}^{(\gamma)}$ is constructed. It is defined as the energy sum of all final state hadrons in the photon hemisphere ($\eta^+ < 0$) in the $\gamma^* I\!P$ CMS which are not associated to the two highest p_T jets, i.e. lie outside the two jet cones in the (η, ϕ) plane. The cross section is shown differentially in $E_{rem}^{(\gamma)}$ in Fig. 10b. The distribution is dominated by small values, indicating the dominance of direct photon scattering. The description at higher $E_{rem}^{(\gamma)}$ values (corresponding to $x_\gamma < 1$) is again much improved by adding the resolved γ^* contribution.

Similar observations are also made for the jet profiles in Fig. 4 and the distribution of the transverse energy flow not associated to the jets shown in Fig. 5. An increased energy flow behind the backward jet, corresponding to the photon direction, and in the $\eta^+ < 0$ hemisphere of the $\gamma^* I\!\!P$ system can be better described if the resolved photon contribution is added, which would not be possible just by adjusting the gluon distribution. The picture of a resolved virtual photon can be viewed as an approximation to next-to-leading order QCD diagrams and/or contributions without strong k_T ordering. The presence of such contributions will be further investigated in section 5.5 .

5.4 Soft Color Neutralization

Soft Color Interactions (SCI) and recently the Semiclassical model have both been able to give a reasonably good description of inclusive diffraction at HERA with a small number of free parameters. In Fig. 11, they are compared with the dijet cross sections as functions of $p^*_{T,jets}$, M_X, $x_{I\!\!P}$ and $z_{I\!\!P}^{(jets)}$. The original version of SCI [25], which gave an acceptable description of $F_2^{D(3)}$ with a single free parameter fixed by the data, also gives a reasonable description of the shapes of the differential distributions of the dijet data, but is too low in normalization. The semi-classical model [15] gives similar results. Both models underestimate the cross sections by a factor of about 2. This is the case even in the region of low $x_{I\!\!P} < 0.01$, where secondary exchanges are negligible.

The refined version of the SCI model [26], based on a generalized area law for string rearrangements, is also compared to the data. It has been shown to give a better description of $F_2^{D(3)}$ at low Q^2. The new version of SCI reproduces the normalization of the dijet cross sections much better. However, the shapes of the differential distributions, such as $\log x_{I\!\!P}$ or $z_{I\!\!P}^{(jets)}$, are not described.

Soft color neutralization models predict the shape and normalizations of the dijet cross sections in leading order QCD approaches based on fits to $F_2^{D(3)}$. The observed disagreement with the measured cross sections may be reduced if next-to-leading order (NLO) calculations were available. Definite conclusions about the validity of these approaches are thus difficult to draw at this stage.

5.5 Colour Dipole and 2-Gluon Exchange Models

In this section, models based on the ideas of dipole cross sections and two-gluon exchange are compared with the dijet data: the Saturation model by Golec-Biernat and Wüsthoff and the calculations by Bartels et al. For this purpose, a restricted data sample with the additional cut

$$x_{I\!\!P} < 0.01 \qquad (21)$$

is studied. The calculations were carried out under the assumption of low $x_{I\!P}$ to avoid the valence quark region in the proton and contributions from secondary Reggeon exchanges. Applying this additional restriction reduces the number of events in the data sample by a factor of approx. 4 .

The resolved Pomeron model implies the presence of a soft Pomeron remnant. The same is true for $q\bar{q}g$ production within the Saturation model, because of the k_T-ordering condition imposed for the calculations. By contrast, the $q\bar{q}g$ calculation of Bartels et al. ("BJLW") relies on high transverse momenta of all particles and is not restricted to k_T-ordered configurations. Any 'remnant' system in this model is expected to have larger p_T. To gain more insight into the properties of the part of the hadronic final state not belonging to the jets, a new observable $p_{T,rem}^{(I\!P)}$ is introduced. Similarly to the definition of $E_{rem}^{(\gamma)}$, which was introduced in section 5.3, this variable measures the transverse momentum of the summed hadronic final state particles in the Pomeron hemisphere of the $\gamma^* I\!P$-CMS not belonging to the two highest p_T jets.

Dijet cross sections for the region $x_{I\!P} < 0.01$ differential in Q^2, $p_{T,jets}^*$, $z_{I\!P}^{(jets)}$ and $p_{T,rem}^{(I\!P)}$ are shown in Fig. 12 . The Saturation model is not able to reproduce the absolute normalization of the data[8], falling short by a factor of approx. 2 except at the highest measured values of Q^2 and p_T^*. It also does not describe the observed shapes of the distributions, e.g. $z_{I\!P}^{(jets)}$. For the BJLW model, the contribution from $q\bar{q}$ states alone is shown scaled by a factor of 5. It is negligibly small except at large values of $z_{I\!P}$. As expected for large values of M_X (low β), the $q\bar{q}g$ contribution is much more significant. The normalization of the BJLW model for $q\bar{q}g$ production is principally controlled by the lower cutoff on the transverse momentum of the gluon in the calculations. If this cutoff is set to $p_{T,g}^2 > 1.0\ \mathrm{GeV}^2$, there is a reasonable description of the overall dijet cross section for $x_{I\!P} < 0.01$. The description of the shapes of the distributions is also reasonable given that there are only two free parameters. The $p_{T,rem}^{(I\!P)}$ distribution is particularly well described. Lowering the gluon transverse momentum cutoff to $p_{T,g}^2 > 0.5\ \mathrm{GeV}^2$ leads to a cross section significantly above the measured data, notably at low $p_{T,rem}^{(I\!P)}$. This behavior and the fact that the Saturation model underestimates the cross section considerably, is suggestive of non-k_T-ordered contributions in the data, as discussed in section 5.3. If the BJLW model is compared to the bulk of the data with $0.01 < x_{I\!P} < 0.05$, it substantially underestimates the cross sections.

5.6 3-Jet Production

The diffractive production of 3 high-p_T jets as components of the X system has been investigated. Except for the requirement on the number of jets, the analysis is identical to the dijet analysis. Again, *inclusive* jet-production is studied, not requiring the absence of hadronic activity beyond the jets. Approximately 130 events are observed for $p_{T,jet}^* > 4\ \mathrm{GeV}$. The statistical precision of the measurement is thus much poorer than for the dijet analysis.

---

[8] It is possible that a fraction of the observed difference between the Saturation and the BJLW models is due to the choices of unintegrated gluon structure functions $\mathcal{F}(x, k_t^2)$ used in the models. The BJLW model uses the NLO parameterization of GRV [46], whereas in the Saturation model $\mathcal{F}$ is parameterized from the fit to the $F_2(x, Q^2)$ data.

In Fig. 13, the measured 3-jet cross sections are presented as functions of two observables, the 3-jet invariant mass M_{123} and

$$z_{I\!P}^{(3\ jets)} = \frac{Q^2 + M_{123}^2}{Q^2 + M_X^2} \ , \tag{22}$$

which is, in analogy to the definition of $z_{I\!P}^{(jets)}$ for dijet events, a measure of the fraction of the energy of the X system which is contained in the jets. The measured cross sections are generally above the predictions from the resolved partonic Pomeron model based on the H1 QCD fits to $F_2^{D(3)}$. The "flat gluon" parton distributions, evaluated at a scale $\mu^2 = Q^2 + p_T^2$, are used. Direct and resolved γ^* contributions are included. Because the leading order for 3-parton final states is $O(\alpha_s^2)$, two different approximations for higher order QCD diagrams are considered here, the Parton Shower model (MEPS) and the Color Dipole model (CDM). The difference between the data and the models may be explained by the lack of a full next-to-leading order treatment of the three-parton final states. The BJLW model with $p_{T,g}^2 = 1.0\ \mathrm{GeV}^2$ is not able to accommodate the observed rate of 3-jet events. However, for kinematic reasons, the 3-jet events have large values of $x_{I\!P} > 0.01$, where contributions from the proton valence region can no longer be neglected.

The cross section differential in $z_{I\!P}^{(3\ jets)}$ demonstrates that additional hadronic activity beyond the jets is typically present even in the 3-jet sample. An improvement in the description of the cross section by dipole models may come through the inclusion of higher multiplicity states such as $q\bar{q}gg$, which have not yet been calculated.

6 Summary and Conclusions

An analysis of the production of jets as components of the dissociating photon system X in the diffractive deep-inelastic scattering reaction $ep \rightarrow eXY$ was presented in the kinematic region $4 < Q^2 < 80\ \mathrm{GeV}^2$, $x_{I\!P} < 0.05$ and $p_T^* > 4\ \mathrm{GeV}$. The values of M_Y and $|t|$ satisfy $M_Y < 1.6\ \mathrm{GeV}$ and $|t| < 1.0\ \mathrm{GeV}^2$. The kinematic range has been extended compared to previous diffractive dijet measurements [7][9] and the statistical precision is much improved. The production of three high transverse momentum jets has also been studied for the first time in diffraction.

The observed dijet events typically exhibit a structure where the X system contains additional hadronic energy with transverse momentum below the jet scale, in addition to the reconstructed jets. The dijet invariant mass is thus generally smaller than M_X. The additional energy is distributed in both hemispheres of the rest frame of X, with a certain preference for the Pomeron hemisphere. This can be interpreted in terms of a dominance of higher multiplicity parton level states (e.g. $q\bar{q}g$) over the simple $q\bar{q}$ configuration.

In a resolved partonic Pomeron model, the dijet data give highly competitive constraints on the diffractive gluon distribution and are also sensitive to the Pomeron intercept $\alpha_{I\!P}(0)$. The data require a large fraction of the Pomeron momentum to be carried by a gluon distribution

---

[9] The principal differences are the lowered Q^2 and $p_{T,jet}^*$ cuts.

which is comparatively flat in $z_{I\!P}$, compatible with the “flat gluon” (or “fit 2”) parameterization in [2]. The data are compatible with a factorisable $x_{I\!P}$ dependence and a value for the Pomeron intercept of $\alpha_{I\!P}(0) \sim 1.2$, significantly higher than the soft Pomeron value of $\alpha_{I\!P}(0) = 1.08$. The dijet cross sections are best described when a contribution from resolved virtual photons of about 17% of the measured cross sections is added. The need for this contribution is confirmed by the observation of enhanced hadronic activity in the photon hemisphere. This contribution can also be considered as a first approximation to NLO QCD terms or to non k_T-ordered contributions.

The Soft Color Interactions model (SCI) and the similarly motivated Semiclassical model are not able to reproduce the dijet cross sections in shape and normalization at the same time. The Semiclassical model and the original SCI model give reasonable descriptions of the shapes of the differential distributions, but underestimate the overall cross sections by a factor of around 2. The area-law-improved version of SCI is better in normalization, but fails to describe the differential distributions.

Models based on colour dipole cross sections and two-gluon exchange have been compared with the dijet data in the restricted kinematic region of $x_{I\!P} < 0.01$. The Saturation model of Golec-Biernat and Wüsthoff, taking only k_T ordered configurations into account, predicts jet cross sections too low in normalization by a factor of approx. 2 . The model of Bartels et al., in which strong k_T ordering is not imposed, is more successful. In this model, $q\bar{q}g$ or higher multiplicity states are dominant at the relatively large M_X values of the present data. With a cutoff for the gluon transverse momentum of $p_{T,g}^2 > 1.0 \text{ GeV}^2$, a reasonable description of the dijet cross sections is obtained in the region $x_{I\!P} < 0.01$. Lower values of this cutoff are disfavored by the data.

For the 3-jet production cross sections, strong conclusions cannot yet be drawn, because of the limited statistical accuracy and the kinematic restriction to large $x_{I\!P}$ implied by the requirement of 3 high p_T jets. Nonetheless, the 3-jet cross sections are found to be significantly above the predictions based on H1 fits to $F_2^{D(3)}$. The 2-gluon model by Bartels et al. is also unable to reproduce the rate of observed 3-jet events.

Diffractive jet production has been shown to be a powerful tool to gain insight into the underlying QCD dynamics of diffraction, in particular the role of gluons. The jet cross sections are sensitive to differences between phenomenological models which all give a reasonable description of $F_2^{D(3)}$. For the first time, a calculation based on 2-gluon exchange has been able to successfully predict low-$|t|$ diffractive dissociation cross sections at HERA in terms of perturbative QCD.

Acknowledgements

We are grateful to the HERA machine group whose outstanding efforts have made and continue to make this experiment possible. We thank the engineers and technicians for their work in constructing and now maintaining the H1 detector, our funding agencies for financial support, the DESY technical staff for continual assistance, and the DESY directorate for the hospitality which they extend to the non DESY members of the collaboration.

References

[1] H1 Collaboration, T. Ahmed *et al.*, *Phys. Lett.* **B 348** (1995) 681.

[2] H1 Collaboration, T. Ahmed *et al.*, *Z. Phys.* **C 76** (1997) 613.

[3] ZEUS Collaboration, J. Breitweg *et al.*, *Eur. Phys. J.* **C 6** (1999) 43;
ZEUS Collaboration, J. Breitweg *et al.*, *Eur. Phys. J.* **C 1** (1998) 81.

[4] UA8 Collaboration, R. Bonino *et al.*, *Phys. Lett.* **B 211** (1988) 239;
UA8 Collaboration, A. Brandt *et al.*, *Phys. Lett.* **B 297** (1992) 417.

[5] CDF Collaboration, T. Affolder *et al.*: *Dijet Production by Double Pomeron Exchange at the Fermilab Tevatron*, FERMILAB-PUB-00/098-E, submitted to *Phys. Rev. Lett.*;
CDF Collaboration, T. Affolder *et al.*, *Phys. Rev. Lett.* **84** (2000) 5043;
CDF Collaboration, F. Abe *et al.*, *Phys. Rev. Lett.* **81** (1998) 5278;
CDF Collaboration, F. Abe *et al.*, *Phys. Rev. Lett.* **80** (1998) 1156;
CDF Collaboration, F. Abe *et al.*, *Phys. Rev. Lett.* **79** (1998) 2636.

[6] D0 Collaboration, B. Abbott *et al.*: *Hard Single Diffraction in $p\bar{p}$ Collisions at 630 and 1800 GeV*, hep-ex/9912061, submitted to *Phys. Rev. Lett.*;
D0 Collaboration, B. Abbott *et al.*, *Phys. Lett.* **B 440** (1998) 189;
D0 Collaboration, S. Abachi *et al.*, *Phys. Rev. Lett.* **76** (1996) 734.

[7] H1 Collaboration, T. Ahmed *et al.*, *Eur. Phys. J.* **C 6** (1999) 421.

[8] ZEUS Collaboration, J. Breitweg *et al.*, *Eur. Phys. J.* **C 5** (1998) 41.

[9] L. Trentadue, G. Veneziano, *Phys. Lett.* **B 323** (1994) 201.

[10] A. Berera, D. Soper, *Phys. Rev.* **D 50** (1994) 4328.

[11] M. Grazzini, L. Trentadue, G. Veneziano, *Nucl. Phys.* **B 519** (1998) 394.

[12] J. Collins, *Phys. Rev.* **D 57** (1998) 3051.

[13] V. Gribov, L. Lipatov, *Sov. J. Nucl. Phys.* **15** (1972) 438, 675;
Yu. Dokshitzer, *JETP* **46** (1977) 641;
G. Altarelli, G. Parisi, *Nucl. Phys.* **B 126** (1977) 298.

[14] F. Hautmann, Z. Kunszt, D.E. Soper, *Phys. Rev. Lett.* **81** (1998) 3333.

[15] W. Buchmüller, T. Gehrmann, A. Hebecker, *Nucl. Phys.* **B 537** (1999) 477.

[16] G. Ingelman, P. Schlein, *Phys. Lett.* **B 152** (1985) 256.

[17] A. Donnachie, P. Landshoff, *Phys. Lett.* **B 296** (1992) 227.

[18] J. Bartels, J. Ellis, H. Kowalski, M. Wüsthoff, *Eur. Phys. J.* **C 7** (1999) 443.

[19] F. Low, *Phys. Rev.* **D 12** (1975) 163;
S. Nussinov, *Phys. Rev. Lett.* **34** (1975) 1286.

[20] A. Mueller, *Nucl. Phys.* **B 335** (1990) 115;
M. Ryskin, Sov. J. Nucl. Phys. **52** (1990) 529;
N. Nikolaev, B. Zakharov, *Z. Phys.* **C 53** (1992) 331;
M. Diehl, *Z. Phys.* **C 66** (1995) 181.

[21] N. Nikolaev, B.G. Zakharov, *Z. Phys.* **C 49** (1990) 607.

[22] K. Golec-Biernat, M. Wüsthoff, *Phys. Rev.* **D 60** (1999) 114023.

[23] J. Bartels, H. Lotter, M. Wüsthoff, *Phys. Lett.* **B 379** (1996) 239;
J. Bartels, C. Ewerz, H. Lotter, M. Wüsthoff, *Phys. Lett.* **B 386** (1996) 389.

[24] J. Bartels, H. Jung, M. Wüsthoff, *Eur. Phys. J.* **C 11** (1999) 111.

[25] A. Edin, G. Ingelman, J. Rathsman, *Phys. Lett.* **B 366** (1996) 371;
A. Edin, G. Ingelman, J. Rathsman, *Z. Phys.* **C 75** (1997) 57.

[26] J. Rathsman, *Phys. Lett.* **B 452** (1999) 364.

[27] H. Jung, *Comp. Phys. Commun.* **86** (1995) 147.
(see also http://www.desy.de/∼jung/rapgap.html)

[28] J. Owens, *Phys. Rev.* **D 30** (1984) 943.

[29] M. Bengtsson, T. Sjöstrand, *Z. Phys.* **C 37** (1988) 465.

[30] T. Sjöstrand, *Comp. Phys. Commun.* **39** (1986) 347;
T. Sjöstrand, M. Bengtsson, *Comp. Phys. Commun.* **43** (1987) 367.

[31] G. A. Schuler, T. Sjöstrand, *Z. Phys.* **C 68** (1995) 607;
G. A. Schuler, T. Sjöstrand, *Phys. Lett.* **B 376** (1996) 193.

[32] H1 Collaboration, C. Adloff *et al.*, *Eur. Phys. J.* **C 13** (2000) 397.

[33] H. Kowalski, *implementation into the RAPGAP program* [27].

[34] F.-P. Schilling, *implementation into the RAPGAP program* [27].

[35] A. Edin, G. Ingelman, J. Rathsman, *Comp. Phys. Commun.* **101** (1997) 108.

[36] F.-P. Schilling, Ph.D. Thesis, University of Heidelberg (Germany), *in preparation*.

[37] H1 Collaboration, I. Abt *et al.*, *Nucl. Instrum. Methods* **A 386** (1997) 310,348.

[38] H1 Collaboration, C. Adloff *et al.*, *Z. Phys.* **C 74** (1997) 221;
H1 Collaboration, C. Adloff *et al.*, *Eur. Phys. J.* **C 1** (1998) 495.

[39] CDF Collaboration, F. Abe *et al.*, *Phys. Rev.* **D 45** (1992) 1448.

[40] H. Spiesberger, H. Möhring, *Comp. Phys. Commun.* **69** (1992) 155.

[41] L. Lönnblad, *Comp. Phys. Commun.* **71** (1992) 15.

[42] B. List: *Diffraktive J/Ψ-Produktion in Elektron-Proton-Stössen am Speicherring HERA*, Diploma Thesis (Tech. Univ. Berlin), 1993 (unpublished);
B. List, A. Mastroberardino 1999: *DIFFVM: A Monte Carlo Generator for diffractive processes in ep scattering* in A. T. Doyle, G. Grindhammer, G. Ingelman, H. Jung (eds.): *Monte Carlo Generators for HERA Physiscs*, DESY-PROC-1999-02, page 396-404.

[43] H1 Collaboration, T. Ahmed *et al.*, *Eur. Phys. J.* **C 1** (1998) 495;
H1 Collaboration, T. Ahmed *et al.*, *Phys. Lett.* **B 428** (1998) 206;
H1 Collaboration, T. Ahmed *et al.*, *Eur. Phys. J.* **C 5** (1998) 3, 439.

[44] ZEUS Collaboration, J. Breitweg *et al.*, *Phys. Lett.* **B 421** (1998) 368.

[45] H1 Collaboration, C. Adloff *et al.*, *Phys. Lett.* **B 483** (2000) 36;
ZEUS Collaboration, J. Breitweg *et al.*, *Eur. Phys. J.* **C 11** (1999) 1,35.

[46] M. Glück, E. Reya, A. Vogt, *Z. Phys.* **C 67** (1995) 433.

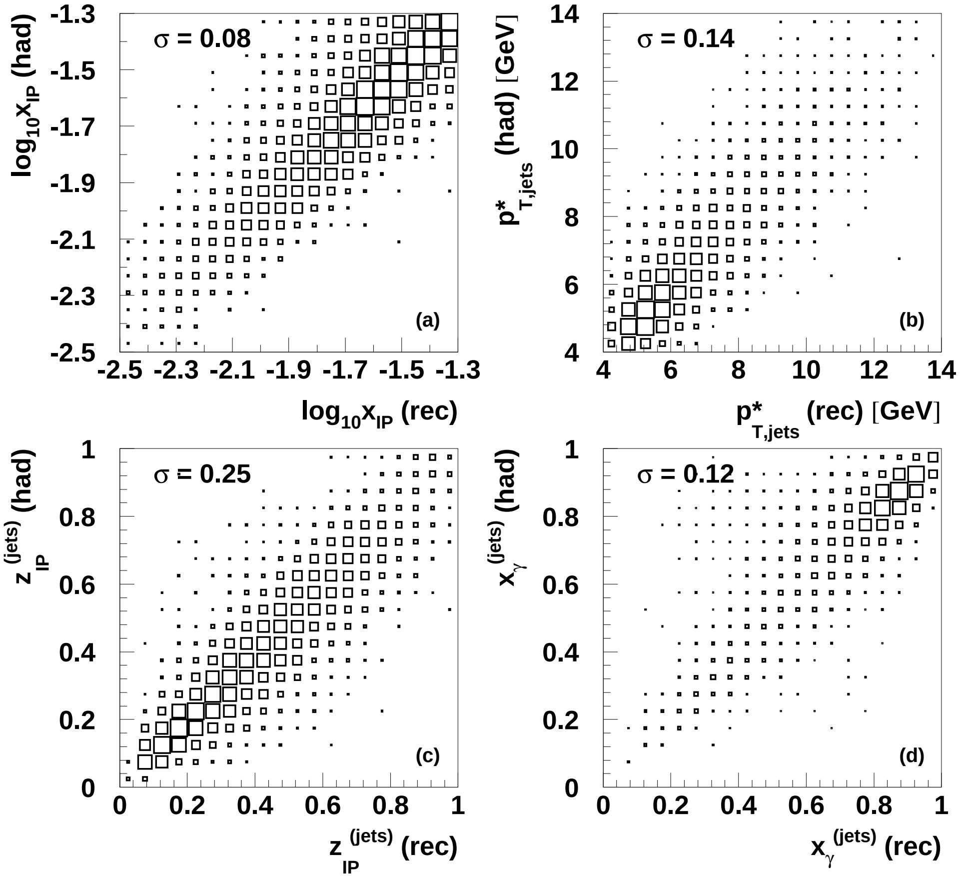

Figure 3: Correlations between the generated hadron level (labelled "had") and the reconstructed level (labeled "rec") values of *(a)* $\log_{10} x_{I\!P}$, *(b)* $p^*_{T,jets}$, *(c)* $z_{I\!P}^{(jets)}$ and *(d)* $x_\gamma^{(jets)}$ for the simulated sample of RAPGAP events as described in section 3.5.

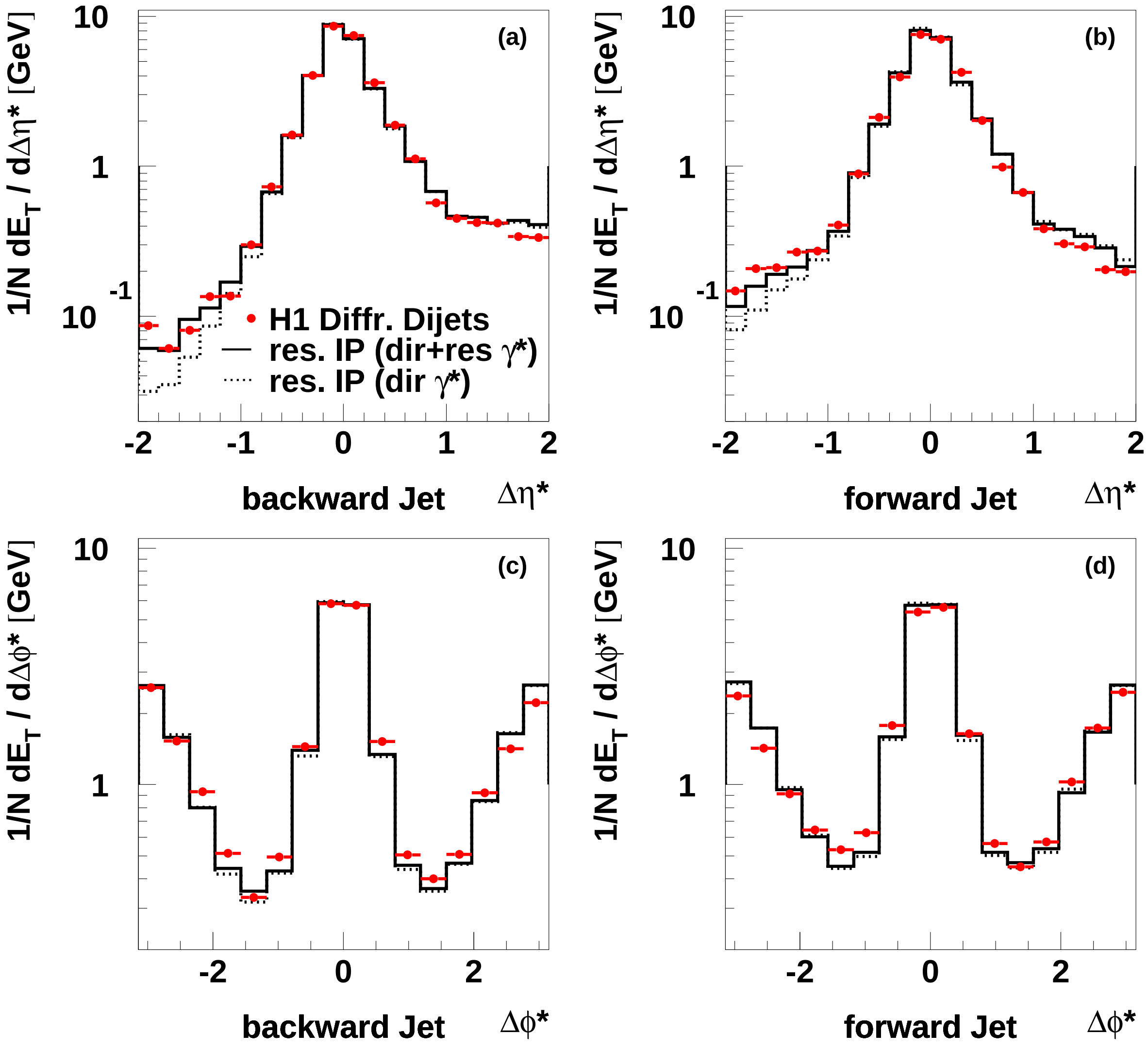

Figure 4: Observed distributions of the average transverse energy flow per event around the jet axes in the diffractive dijet sample. $\Delta\eta^*$ and $\Delta\phi^*$ are the distances from the jet axes in pseudorapidity and azimuthal angle in the hadronic center-of-mass frame. The jet profiles in η and ϕ are integrated over ±1 unit in ϕ and η respectively. *(a)* and *(c)* show the distributions for the backward jet in the laboratory frame, whereas *(b)* and *(d)* show those for the forward jet. For comparison, the distributions for the simulated sample of RAPGAP events are also shown. Here, the contribution from direct photons only and the sum of direct and resolved photon contributions are shown.

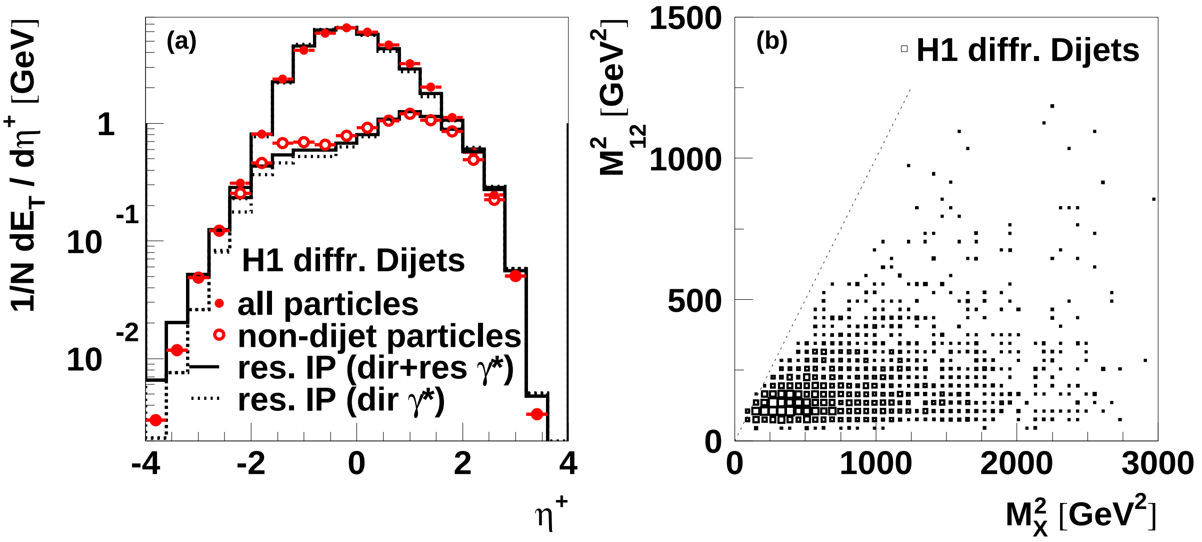

Figure 5: *(a)* The uncorrected distribution of the average transverse energy per event in the $\gamma^* I\!\!P$ center-of-mass frame as a function of the pseudorapidity η^+ for the diffractive dijet sample. Shown are the distributions for all final state particles *(solid points)* and for only those particles which do not belong to the two highest p_T jets *(open points)*. The prediction of the RAPGAP simulations for either direct or direct plus resolved virtual photon contributions are also shown. *(b)* The uncorrected correlation between the invariant mass of the X system squared M_X^2 and the dijet invariant mass squared M_{12}^2 for the diffractive dijet sample. The dotted line corresponds to $M_X^2 = M_{12}^2$.

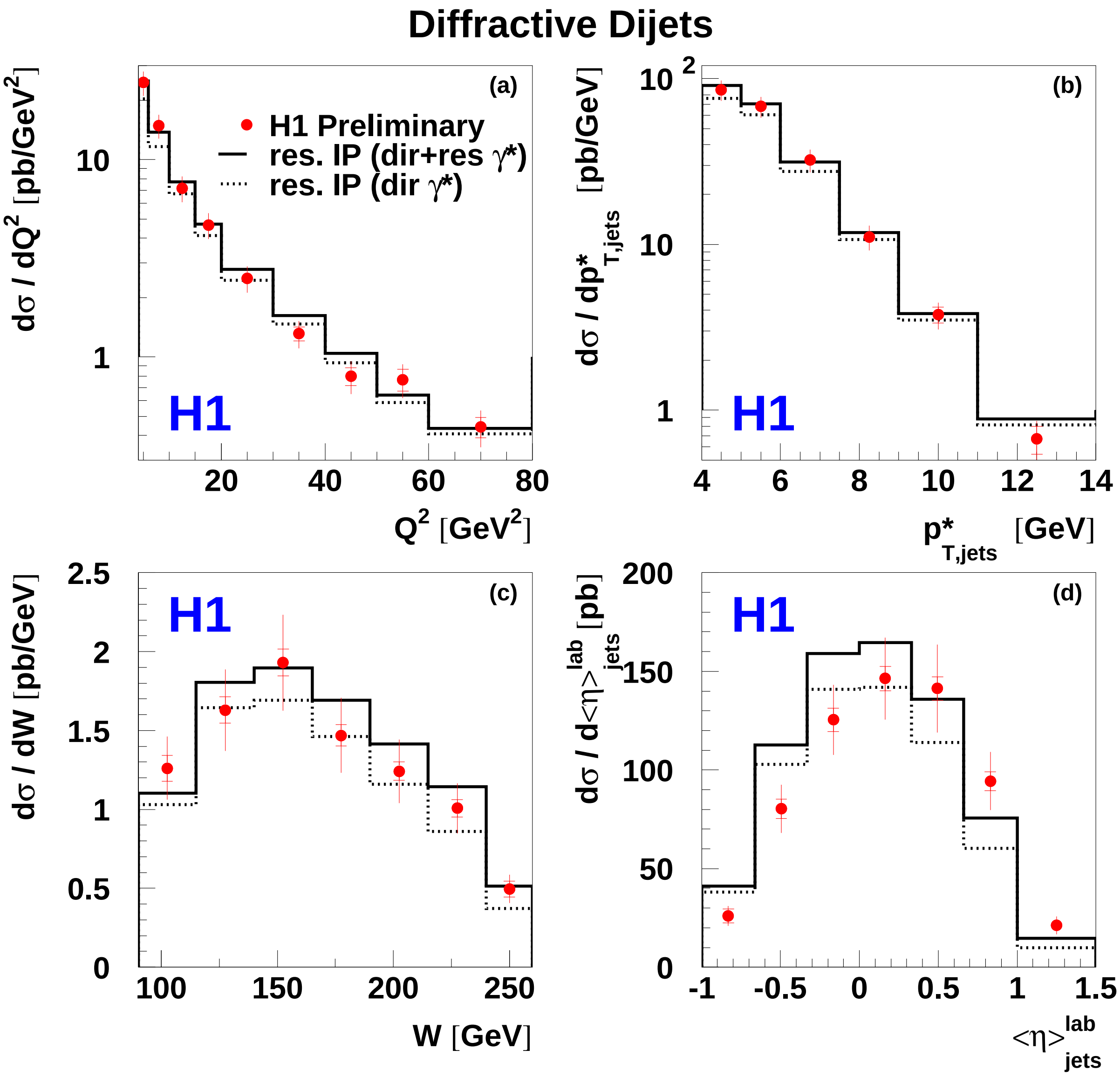

Figure 6: Diffractive dijet cross sections as a function of *(a)* the photon virtuality Q^2, *(b)* the mean transverse jet momentum $p^*_{T,jets}$, *(c)* the $\gamma^* p$ invariant mass W and *(d)* the mean jet pseudorapidity in the lab frame $\langle\eta\rangle^{lab}_{jets}$. Also shown are the predictions from a resolved (partonic) Pomeron model with gluon dominated Pomeron parton distributions as obtained from the QCD analysis of $F_2^{D(3)}$ by H1 [2]. Here, the “fit 2” parton distributions for the Pomeron were used, evolved to a scale $\mu^2 = Q^2 + p_T^2$. The dotted line corresponds to the direct virtual photon cross section, whereas for the solid line direct and resolved γ^* contributions according to the SaS-2D parameterization have been added.

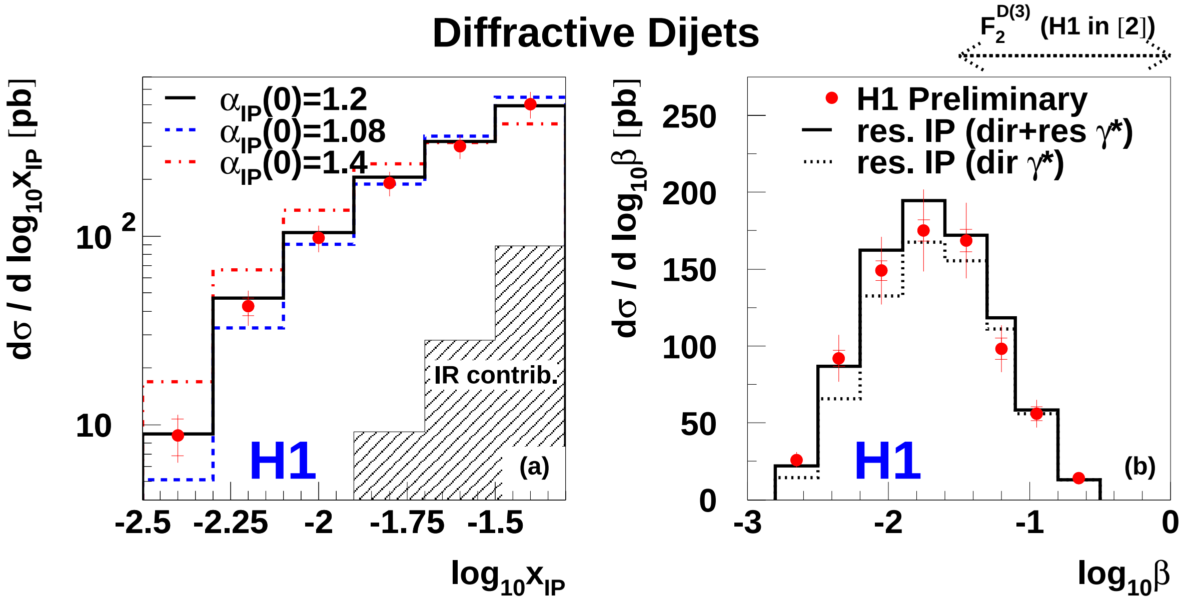

Figure 7: Differential diffractive dijet cross sections as a function of *(a)* the longitudinal proton momentum fraction of the colorless exchange $x_{I\!P}$ and *(b)* β, the longitudinal momentum fraction of the exchange carried by the quark coupling to the photon. The solid curves represent the predictions of the resolved Pomeron model as described in the text with direct and resolved photon contributions. For the $\log_{10} x_{I\!P}$ distribution, the contribution from sub-leading Reggeon exchange within a resolved Pomeron model, based on the H1 fits to $F_2^{D(3)}$ in [2], is indicated by the hatched area. The dashed and dashed-dotted curves correspond to the cross section predictions where the value of the Pomeron intercept $\alpha_{I\!P}(0)$ in the model was changed from the default value of 1.20 to 1.08 and 1.40 respectively while the normalization was kept fixed. For the β distribution, the contribution from direct photons only is also shown and the range covered by the inclusive H1 measurement of $F_2^{D(3)}$ is indicated.

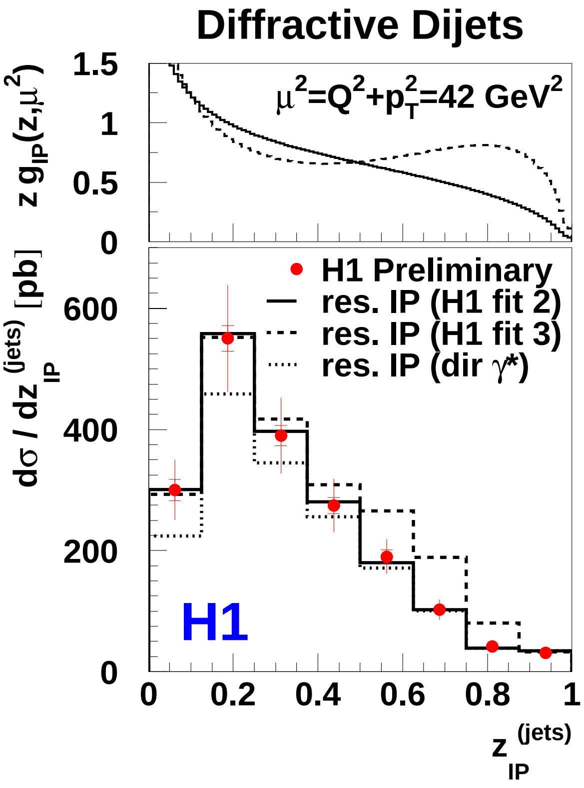

Figure 8: The diffractive dijet cross section as a function of $z_{I\!P}^{(jets)}$, corresponding within a partonic Pomeron model to the Pomeron momentum fraction which enters the hard scattering process. The predictions of the resolved Pomeron model for two different parameterizations of the Pomeron gluon density, obtained from the H1 QCD fits to $F_2^{D(3)}$ [2], are also shown, namely the "flat gluon" (labeled "H1 fit 2") and the "peaked gluon" (labeled "H1 fit 3") distributions. These gluon distributions, evolved to a scale $\mu^2 = Q^2 + p_T^2 = 42\ \mathrm{GeV}^2$, corresponding to the mean value of the event sample, are also shown. The model predictions are shown for the sum of direct and resolved photon contributions. The size of the direct photon contribution alone is indicated by the dotted line.

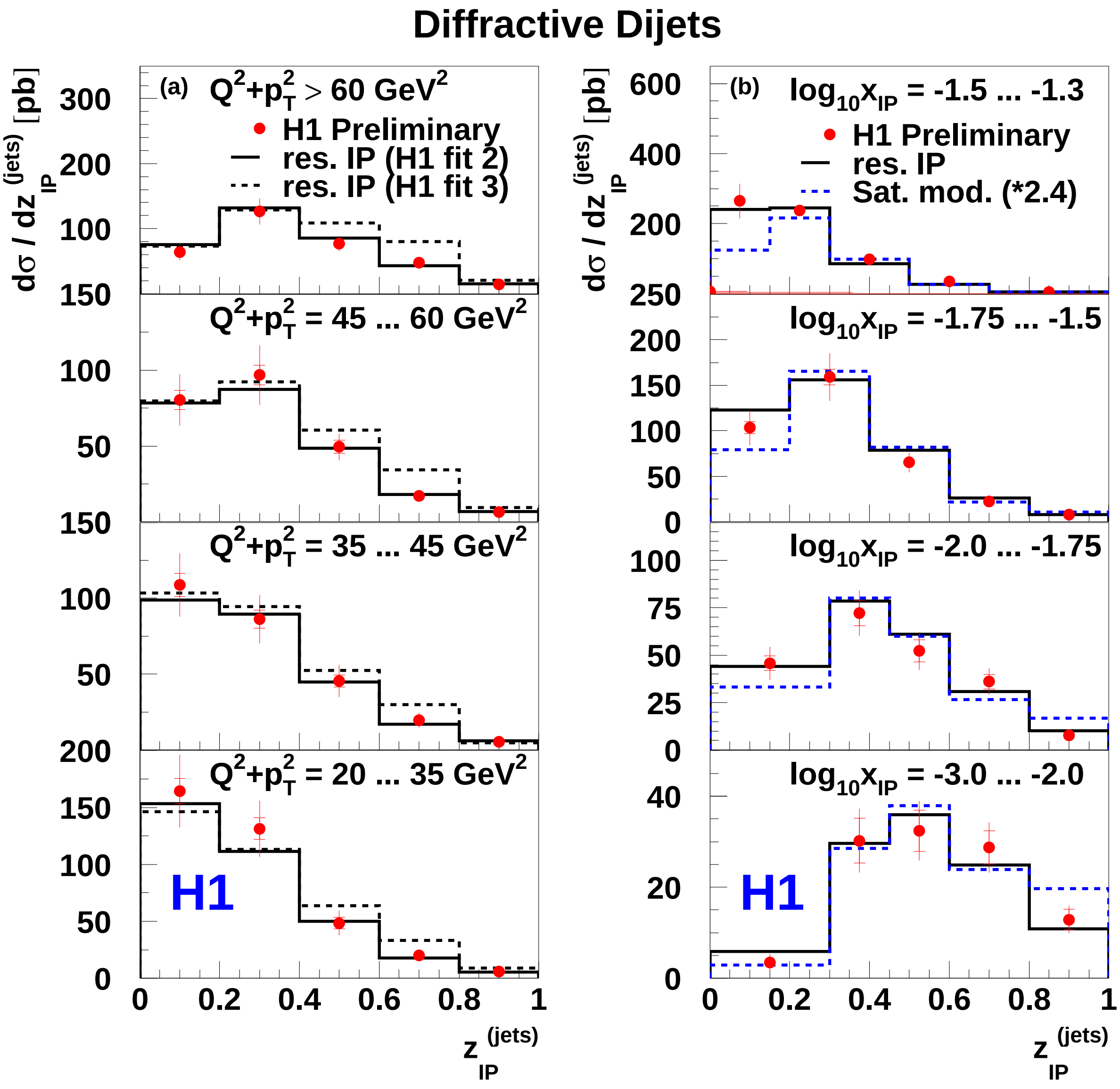

Figure 9: *(a)* Diffractive dijet cross sections as a function of $z_{I\!P}^{(jets)}$, shown in four bins of the scale $\mu^2 = Q^2 + p_T^2$. The data are compared to the resolved Pomeron model based on the two fits to $F_2^{D(3)}$ from H1, adding direct and resolved γ^* contributions. *(b)* The $z_{I\!P}^{(jets)}$ cross section in four bins of $\log_{10} x_{I\!P}$. Also shown are the predictions from the resolved Pomeron model, where the "H1 fit 2" parameterization was used and direct and resolved γ^* contributions are added, and the Saturation model, scaled by a constant factor of 2.4.

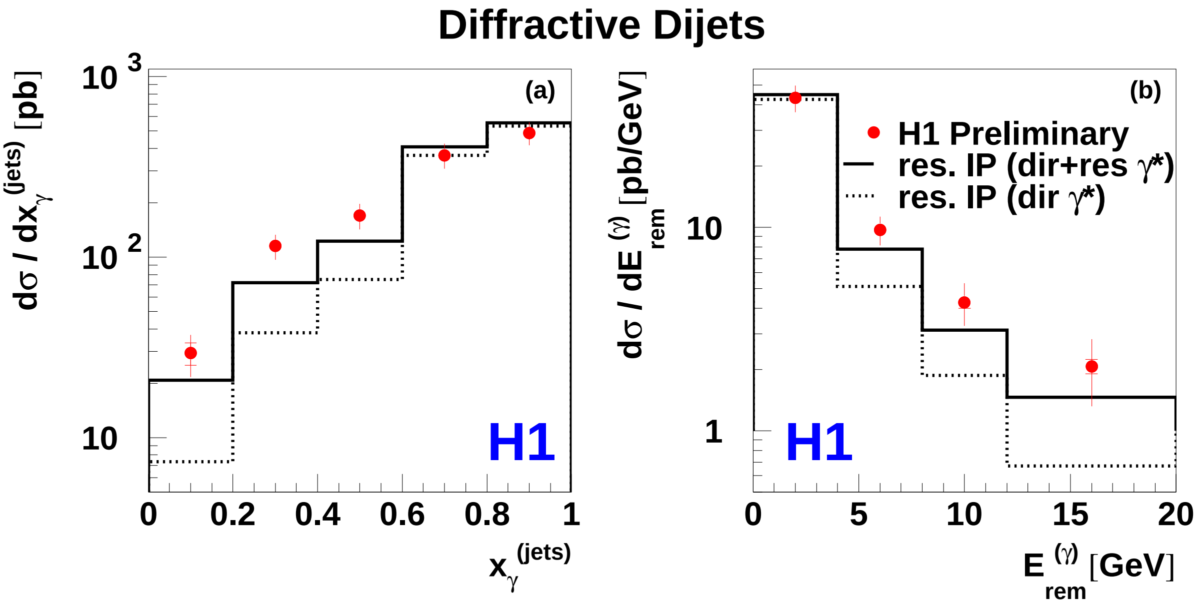

Figure 10: Differential diffractive dijet cross sections as a function of *(a)* $x_\gamma^{(jets)}$, an estimator for the photon momentum fraction entering the hard scattering process, and *(b)* $E_{rem}^{(\gamma)}$, the summed hadronic final state energy, not belonging to the two highest p_T jets, in the photon hemisphere of the $\gamma^* I\!P$-CMS. The data are compared to the resolved Pomeron model with and without an additional contribution from resolved virtual photons, parameterized according to the SaS-2D photon parton distributions.

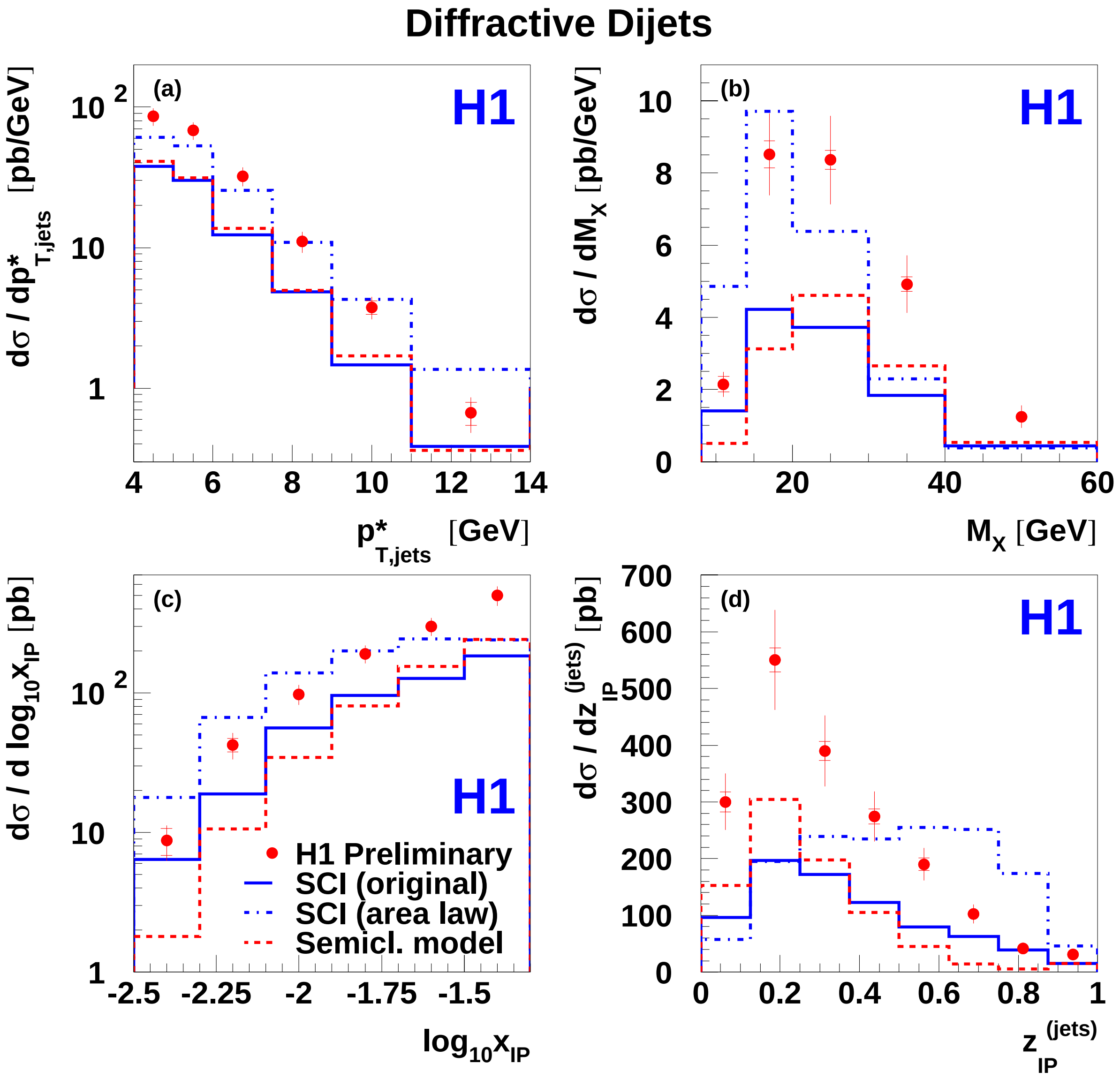

Figure 11: Differential dijet cross sections as functions of *(a)* $p^*_{T,jets}$, *(b)* M_X, *(c)* $\log_{10} x_{I\!P}$ and *(d)* $z_{I\!P}^{(jets)}$. The data are compared to the original version of the Soft Color Interaction (SCI) model, labeled "SCI (original)", the prediction of the improved SCI version based on a generalized area law for string reconnections, labeled "SCI (area law)", and to the Semiclassical model.

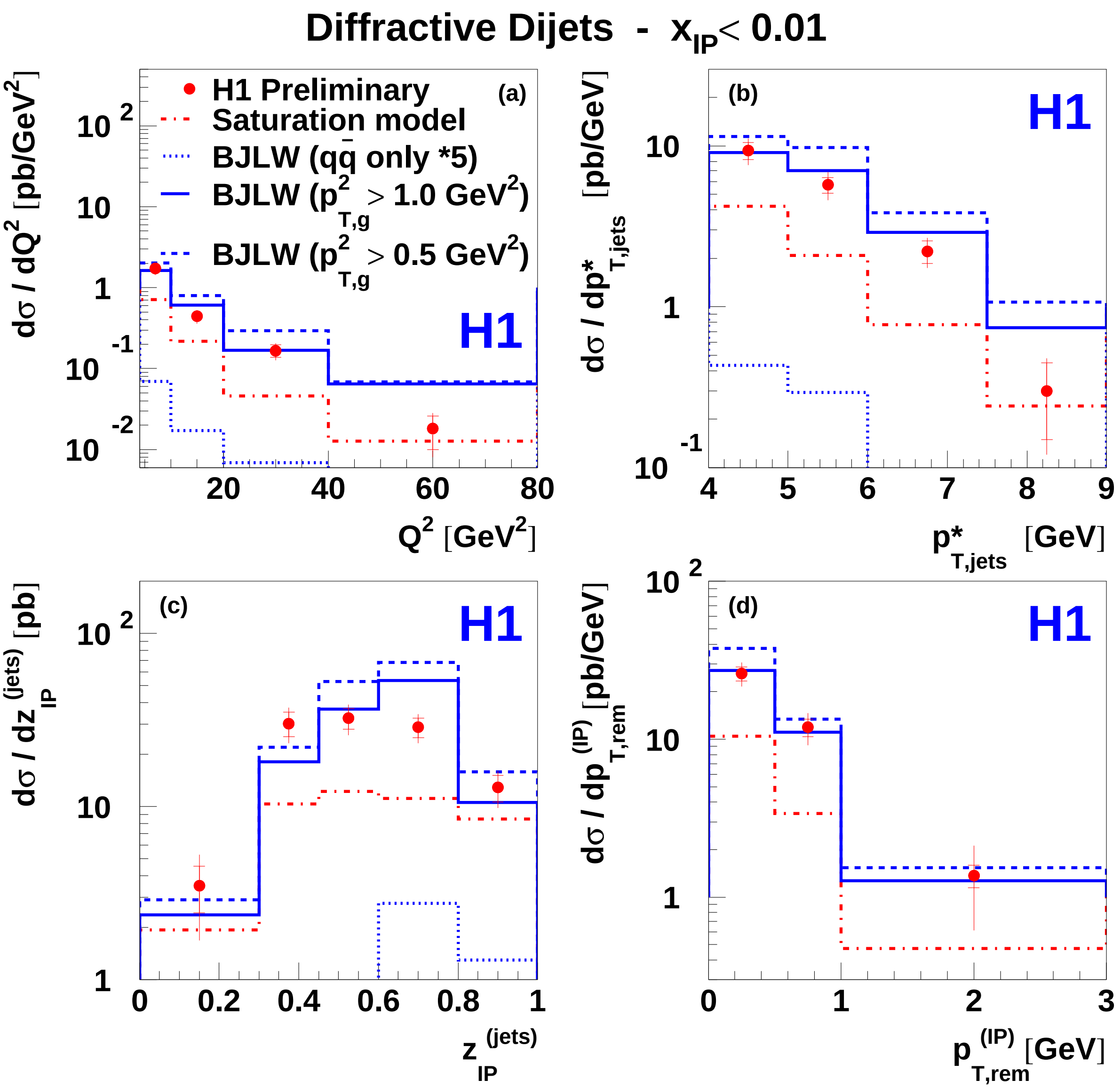

Figure 12: Diffractive dijet cross sections in the restricted kinematic range $x_{I\!P} < 0.01$, shown as functions of *(a)* Q^2, *(b)* $p^*_{T,jets}$, *(c)* $z^{(jets)}_{I\!P}$ and *(d)* $p^{(I\!P)}_{T,rem}$, denoting the summed transverse momentum of the final state particles not belonging to the two highest p_T jets and located in the Pomeron hemisphere of the $\gamma^* I\!P$-CMS. The data are compared to the Saturation model and to the calculations by Bartels et al. (labeled "BJLW"). There, the contribution from $q\overline{q}$ states alone, scaled by a factor of 5, and the sum of the $q\overline{q}$ and $q\overline{q}g$ contributions for two different values of the p_T-cutoff for the gluon in the case of $q\overline{q}g$ production are shown.

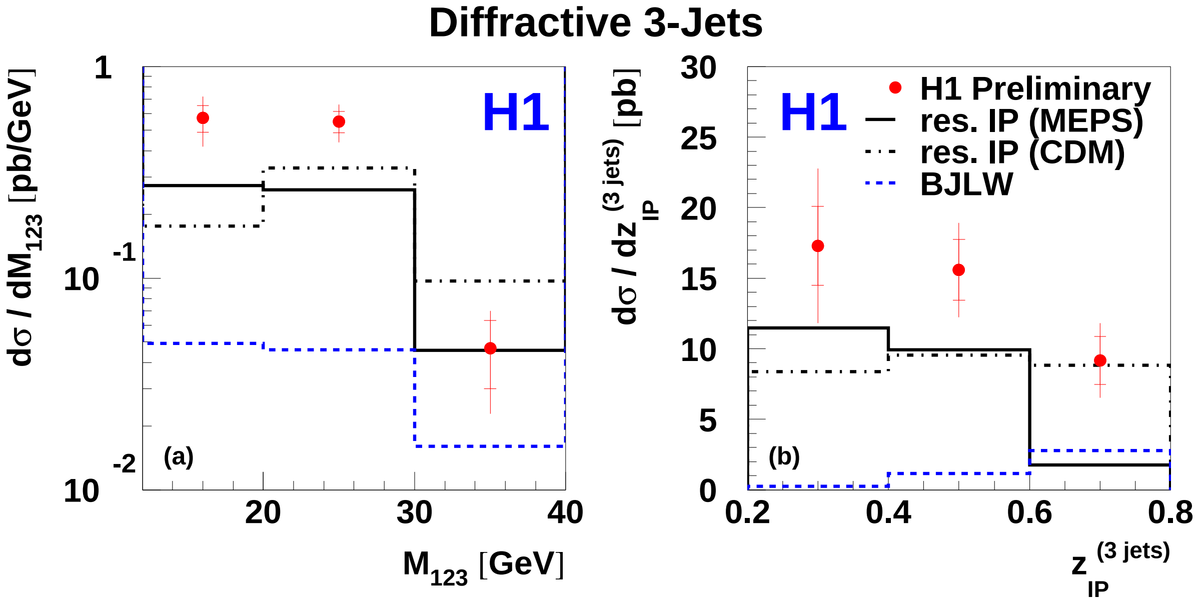

Figure 13: Differential cross sections for diffractive 3-jet production as functions of *(a)* the 3-jet invariant mass M_{123} and *(b)* the corresponding $z_{I\!P}$-variable $z_{I\!P}^{(3\ jets)}$, measuring the colorless exchange momentum fraction which enters the hard interaction. The data are compared to the resolved Pomeron model with two different approaches for higher order QCD diagrams, the Parton Shower model (labeled “MEPS”) and the Color Dipole model (labeled “CDM”). The “H1 fit 2” parameterization is used and direct and resolved virtual photon contributions are added. Also shown is the 2-gluon exchange model by Bartels et al. (labeled “BJLW”), where $q\bar{q}$ and $q\bar{q}g$ contributions are added and the cutoff for the gluon p_T is set to $p_{T,g}^2 > 1.0\ \mathrm{GeV}^2$.